

# Minimal Cooling of Neutron Stars: A New Paradigm

Dany Page

*Departamento de Astrofísica Teórica, Instituto de Astronomía, UNAM, 04510 Mexico D.F., Mexico*  
 page@astroscu.unam.mx

James M. Lattimer

*Department of Physics and Astronomy, State University of New York at Stony Brook, Stony Brook, NY-11794-3800, USA*  
 lattimer@mail.astro.sunysb.edu

Madappa Prakash

*Department of Physics and Astronomy, State University of New York at Stony Brook, Stony Brook, NY-11794-3800, USA*  
 prakash@snare.physics.sunysb.edu

Andrew W. Steiner

*School of Physics and Astronomy, University of Minnesota, Minneapolis, MN 55455, USA*  
 stein@physics.umn.edu

## ABSTRACT

A new classification of neutron star cooling scenarios, involving either “minimal” cooling or “enhanced” cooling is proposed. The minimal cooling scenario replaces and extends the so-called standard cooling scenario to include neutrino emission from the Cooper pair breaking and formation process. This emission dominates that due to the modified Urca process for temperatures close to the critical temperature for superfluid pairing. Minimal cooling is distinguished from enhanced cooling by the absence of neutrino emission from any direct Urca process, due either to nucleons or to exotica such as hyperons, Bose condensates or deconfined quarks. Within the minimal cooling scenario, theoretical cooling models can be considered to be a four parameter family involving the equation of state (including various compositional possibilities) of dense matter, superfluid properties of dense matter, the composition of the neutron star envelope, and the mass of the neutron star. The consequences of minimal cooling are explored through extensive variations of these parameters. The results are compared with the inferred properties of thermally-emitting neutron stars in order to ascertain if enhanced cooling occurs in any of them.

All stars for which thermal emissions have been clearly detected are at least marginally consistent with the lack of enhanced cooling, given the combined uncertainties in ages and temperatures or luminosities. The two pulsars PSR 0833-45 (Vela) and PSR 1706-44 would require enhanced cooling in case their ages and/or temperatures are on the lower side of their estimated values whereas the four stars PSR 0656+14, PSR 1055-52, Geminga, and RX J0720.4-3125 may require some source of internal heating in case their age and/or luminosity are on the upper side of their estimated values. The new upper limits on the thermal luminosity of PSR J0205+6449 (in the supernova remnant 3C58) and RX J0007.0+7302 (in CTA 1) are indicative of the occurrence of some enhanced neutrino emission beyond the minimal scenario.

*Subject headings:* Dense matter — equation of state — neutrinos — stars: neutron

## 1. INTRODUCTION

Within the last several years, several candidates for thermally-emitting neutron stars have been discovered (see, e.g., Pavlov & Zavlin (2002) for a short review). These stars are presumably cooling through the combination of neutrino emission from the interior and photon cooling from the surface, the latter responsible for their observed thermal emissions. Their temperatures have been deduced by fitting atmosphere models to their spectra whereas ages can be inferred from kinematics or from the associated pulsar spin-down timescale. Neutron star cooling depends upon the equation of state (EOS) of dense matter as well as the neutron star mass and their envelope composition. It has been hoped that comparing theoretical cooling curves, i.e., the temperature-age or luminosity-age relation for neutron stars, with observations could yield information about their internal properties.

A goal of this paper to explore how observations of thermal emission from neutron stars might be able to constrain the equation of state of dense matter. We will treat theoretical neutron star cooling trajectories as a four parameter series of models. The parameters are:

- (1) the equation of state (including various compositional possibilities),
- (2) superfluid properties of the relevant components,
- (3) the envelope composition, and
- (4) the stellar mass.

In nature, only one equation of state and one set of superfluid properties is realized, but at the present time, the theoretical range of superfluid properties for a given equation of state is so broad that these must be treated as an independent parameter. In the future, as more observations become available, it should be possible to eliminate some combinations of EOS and superfluid parameter sets, if not entire families of possibilities. It is also not known if a neutron star's envelope composition is unique (at least for a given mass) or if it varies from star to star or as a function of time. The neutron star mass is constrained to lie between the maximum mass (a function of the equation of state) and a minimum mass of about  $1.1 M_{\odot}$  (set by theoretical considerations of neutron

star birth (see, e.g., Burrows & Lattimer (1986))).

Historically, theoretical neutron star cooling models have fallen into two categories, “standard” cooling or enhanced cooling. The so-called “standard cooling” scenario has no “enhanced cooling” which could result from any of the direct Urca processes involving nucleons, hyperons, meson condensates or quark matter (see, e.g. Pethick (1992) and Prakash (1998)). Until recently, “standard” cooling has been treated as being dominated by the modified Urca process (Friman & Maxwell 1979). However, in the presence of superconductivity or superfluidity in the neutron star interior, an additional source of neutrino emission, Cooper pair breaking and formation, occurs (Flowers, Ruderman & Sutherland 1976; Voskresensky & Senatorov 1987). For temperatures near the associated gap energies, Cooper pairs, in fact, dominate the neutrino emissivities. Although the magnitude of the superfluid gap energies as a function of density is somewhat uncertain at present, it is generally accepted that superfluidity occurs in neutron star matter. For this reason, we embark on the “minimal cooling” scenario in which “standard cooling” is extended to include the effects of superfluidity, including Cooper pair breaking and formation.

The purpose of this paper is to explore in as complete a fashion as possible the consequences of this minimal cooling paradigm, employing the four kinds of parameters described above, and to compare our results with the inferred properties of cooling neutron stars. In this way, it will become apparent to what extent one or more of the so-called enhanced cooling mechanisms might be necessary to understand the observations. A future paper will explore in a similar fashion the consequences of enhanced cooling.

One consequence of the minimal cooling paradigm, that enhanced cooling will not occur, is a restriction upon the equation of state involving the symmetry energy. It is well-known (see, e.g., Lattimer et al. (1991)) that the density dependence of the nuclear symmetry energy controls the charge fraction in uniform beta-equilibrium matter. Since the direct Urca process occurs in uniform beta-equilibrium matter when the charge fraction exceeds  $1/9$  (in the absence of muons or hyperons), minimal cooling thus restricts the density dependence of the nuclear symmetry energy: the critical density for the onset of the direct Urca pro-

cess must remain above the star’s central density. When muons are considered, this critical density, for a given equation of state, is slightly lowered. The appearance of hyperons can also trigger other direct Urca processes (Prakash et al. 1992). Thus, to the extent that minimal cooling can explain existing observations, a constraint on the equation of state could be inferred.

In § 2, observations of cooling neutron stars are reviewed. The input physics, including the equation of state, superfluid properties, and neutrino emissivities are discussed in § 3. The influence of the neutron star envelope is briefly discussed in § 4. The results of cooling calculations for minimal cooling models are extensively discussed in § 5. The coldest stars possible within the minimal cooling scenario are identified in § 6 and § 7 contains a summary of the confrontation of the minimal cooling paradigm with existing data. A comparison with other studies is performed in § 8. Conclusions are offered in § 9.

## 2. DATA ON COOLING NEUTRON STARS

Observations of neutron stars whose thermal emission has been unambiguously detected give rise to the information summarized in Tables 1 and 2 whereas Table 3 contains results about objects for which only upper limits have been set. Tables 1 and 2 display four inferred quantities: the total thermal luminosity  $L_\infty$ , the surface temperature  $T_\infty$ , the distance  $d$  and the age  $t$ , whereas Table 3 omits  $T_\infty$ . The subscript  $\infty$  refers to quantities observed at the Earth which are redshifted relative to their values at the stellar surface. The data in these tables are taken from references that are detailed in Appendix A. In cases where a range of estimates is presented in these references, the particular parameters selected for inclusion in these tables are elaborated in Appendix A. Table 1 presents properties as inferred from models incorporating atmospheres dominated by hydrogen, whereas Table 2 presents properties inferred from blackbody or heavy-element dominated atmospheres. The stars displayed in Table 1 are a subset of those in Table 2 because the inferred radii of the excluded stars are far above theoretically plausible values for neutron star radii (see discussion below). The objects listed in Table 3

are fainter than those listed in the first two tables and the upper limits listed have been obtained only very recently thanks to the extended capabilities of *XMM-Newton* and *Chandra*. As a result, much less information has been obtained and the data analysis has not been as detailed as for the stars in Table 1 and 2. Moreover, in four cases no compact object has been detected. Indicated by a “?” in Table 3, these compact remnants may contain isolated black holes instead of neutron stars.

For the purposes of restricting cooling models, we will not use two of these sources. RBS 1223 is suspected of being a magnetar, judging from its inferred extremely high magnetic field. In addition, its period derivative is highly uncertain. RX J0720.4-3125 has a very uncertain age estimate, and both objects possibly have additional heating sources compared to the other sources. RX J0720.4-3125 will be included in the relevant figures, however, for purposes of comparison.

### 2.1. Temperatures

The estimation of  $L_\infty$  and  $T_\infty$  from the observed spectral fluxes requires atmospheric modeling in which three additional factors are involved: the composition of the atmosphere, the column density of x-ray absorbing material between the star and the Earth, and the surface gravitational redshift (the surface gravity does not play a major role in fitting broad spectral flux distributions). The column density is important because the bulk of the emitted flux from neutron stars is absorbed (mostly by interstellar hydrogen) before it reaches the Earth. The surface gravitational redshift, although not a factor in blackbody models, can influence heavy-element atmosphere models. In many references, the gravitational redshift was not optimized, but was set to the canonical value 0.304 implied by  $M = 1.4 M_\odot$  and  $R = 10$  km.

Since narrow spectral lines are not observed in any of the stars in Tables 1 and 2, the atmospheric composition of these neutron stars is unknown. However, some information can be deduced from the shape of the spectral distribution. Broadly speaking, neutron star atmospheres can be described as being either light-element (i.e., H or He) or heavy-element dominated. Heavy-element atmospheres have spectral distributions more closely resembling the blackbody distribution than do light-element atmospheres (Romani

TABLE 1  
NEUTRON STAR PROPERTIES WITH HYDROGEN ATMOSPHERES

Star	$\log_{10} t_{sd}$ yr	$\log_{10} t_{kin}$ yr	$\log_{10} T_{\infty}$ K	$d$ kpc	$\log_{10} L_{\infty}$ erg/s
RX J0822-4247	3.90	$3.57^{+0.04}_{-0.04}$	$6.24^{+0.04}_{-0.04}$	1.9 – 2.5	33.85 – 34.00
1E 1207.4-5209	$5.53^{+0.44}_{-0.19}$	$3.85^{+0.48}_{-0.48}$	$6.21^{+0.07}_{-0.07}$	1.3 – 3.9	33.27 – 33.74
RX J0002+6246	–	$3.96^{+0.08}_{-0.08}$	$6.03^{+0.03}_{-0.03}$	2.5 – 3.5	33.08 – 33.33
PSR 0833-45 (Vela)	4.05	$4.26^{+0.17}_{-0.31}$	$5.83^{+0.02}_{-0.02}$	0.22 – 0.28	32.41 – 32.70
PSR 1706-44	4.24	–	$5.8^{+0.13}_{-0.13}$	1.4 – 2.3	31.81 – 32.93
PSR 0538+2817	4.47	–	$6.05^{+0.10}_{-0.10}$	1.2	32.6 – 33.6

References are cited in Appendix A

TABLE 2  
NEUTRON STAR PROPERTIES WITH BLACKBODY ATMOSPHERES

Star	$\log_{10} t_{sd}$ yr	$\log_{10} t_{kin}$ yr	$\log_{10} T_{\infty}$ K	$R_{\infty}$ km	$d$ kpc	$\log_{10} L_{\infty}$ erg/s
RX J0822-4247	3.90	$3.57^{+0.04}_{-0.04}$	$6.65^{+0.04}_{-0.04}$	1 – 1.6	1.9 – 2.5	33.60 – 33.90
1E 1207.4-5209	$5.53^{+0.44}_{-0.19}$	$3.85^{+0.48}_{-0.48}$	$6.48^{+0.01}_{-0.01}$	1.0 – 3.7	1.3 – 3.9	32.70 – 33.88
RX J0002+6246	–	$3.96^{+0.08}_{-0.08}$	$6.15^{+0.11}_{-0.11}$	2.1 – 5.3	2.5 – 3.5	32.18 – 32.81
PSR 0833-45 (Vela)	4.05	$4.26^{+0.17}_{-0.31}$	$6.18^{+0.02}_{-0.02}$	1.7 – 2.5	0.22 – 0.28	32.04 – 32.32
PSR 1706-44	4.24	–	$6.22^{+0.04}_{-0.04}$	1.9 – 5.8	1.8 – 3.2	32.48 – 33.08
PSR 0656+14	5.04	–	$5.71^{+0.03}_{-0.04}$	7.0 – 8.5	0.26 – 0.32	32.18 – 32.97
PSR 0633+1748 (Geminga)	5.53	–	$5.75^{+0.04}_{-0.05}$	2.7 – 8.7	0.123 – 0.216	30.85 – 31.51
PSR 1055-52	5.43	–	$5.92^{+0.02}_{-0.02}$	6.5 – 19.5	0.5 – 1.5	32.07 – 33.19
RX J1856.5-3754	–	$5.70^{+0.05}_{-0.25}$	5.6 – 5.9	> 16	0.105 – 0.129	31.44 – 31.68
RX J0720.4-3125	$6.0 \pm 0.2$	–	5.55 – 5.95	5.0 – 15.0	0.1 – 0.3	31.3 – 32.5

References are cited in Appendix A

TABLE 3  
PROPERTIES OF BARELY DETECTED OR UNDETECTED OBJECTS

Star (SNR)	$\log_{10} t_{sd}$ yr	$\log_{10} t_{kin}$ yr	$d$ kpc	$\log_{10} L_{\infty}$ erg/s
CXO J232327.8+584842 (Cas A)	-	2.51	3.3 – 3.6	< 34.5
J0205+6449 (3C 58)	3.74	2.91	2.6 – 3.2	< 33.0
PSR J1124-5916 (G292.0+1.8)	3.45	3.15 – 3.30	5 – 6	< 33.3
RX J0007.0+7302 (CTA 1)	-	4.0 – 4.2	1.1 – 1.7	< 32.3
? (G084.2-0.8)	-	3.5 – 4.0	$\approx 4.5$	< 30.68 – 31.45
? (G093.3-6.9)	-	3.3 – 4.0	2.1 – 2.9	< 30.65 – 31.55
? (G127.1+0.5)	-	3.3 – 3.9	1.2 – 1.3	< 29.6 – 30.75
? (G315.4-2.3)	-	3.5 – 4.17	2.4 – 3.2	< 30.65 – 31.80
PSR J0154+61	5.29	-	1.7 – 2.2	< 32.14

References are cited in Appendix A

1987). This is due to the higher opacities of heavy elements, and seems to be the case even in the presence of strong magnetic fields. Since the wavelength range of available x-ray spectra is relatively small, it is possible to fit x-ray spectra with both kinds of atmosphere models. In general, an x-ray spectrum that is fit with a light-element atmosphere will predict the star to have a lower temperature and a larger angular size than will be the case if a heavy-element atmosphere or blackbody is assumed. If the distance is known, the neutron star radius can be inferred (see more on this in § 2.3). In some cases, fitting a star with a light-element atmosphere results in a predicted neutron star radius much larger than the canonical range of 10–15 km. In other cases, fitting a star with a heavy-element atmosphere could result in an inferred radius that is too small.

Chang & Bildsten (2003a,b) have discussed a trend observed from atmospheric modeling of thermal neutron star spectra (Pavlov 2000): the inferred neutron star radii for stars younger than about  $10^5$  years are consistent with canonical values only if they are modeled with light-element atmospheres (magnetized or non-magnetized). Stars older than about  $10^5$  years, on the other hand, have inferred radii close to the canonical range only when modeled with heavy-element atmospheres. For this reason, Table 1 is limited to stars with ages less than about  $10^5$  years, and it displays

results inferred from modeling them with H atmospheres. Table 2, on the other hand, lists all stars, and displays properties deduced from blackbody (or heavy-element dominated) models. The temperatures and luminosities are plotted in Figure 1, and are also selected according to this trend and our desire that the inferred stellar radius lies in a theoretically plausible range. The temperature and luminosity are taken from Table 2 unless values for them appear in Table 1.

The above trend implies that the atmospheric composition of a neutron star evolves from light to heavy elements with a timescale of about  $10^5$  years. This possible evolution is considered in more detail in § 5.2.

## 2.2. Ages

The precise ages of observed cooling neutron stars are not always known. Most stars listed in Tables 1 through 3 are known radio and/or x-ray pulsars and their ages can be estimated from the observed spin-down rate using  $t_{sd} \equiv P/2\dot{P}$ , where  $P$  and  $\dot{P}$  are the period and its time derivative, respectively. In some cases, kinematic information is available and ages can be inferred by relating pulsar transverse velocities to the distances from the presumed sites of origin as, e.g., the geometric center of the associated supernova remnant or a nearby cluster of massive OB stars. In the case of an association with a supernova rem-

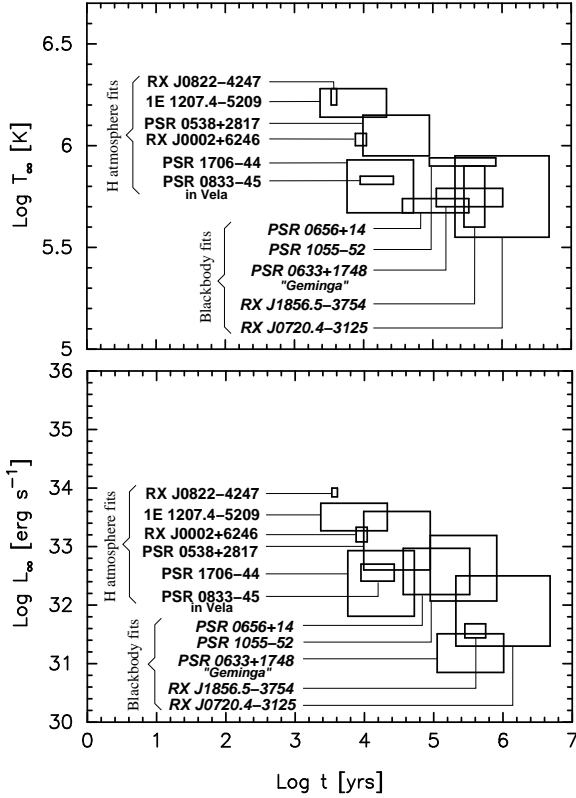


Fig. 1.— Inferred temperature  $T_\infty$  (top) and luminosity  $L_\infty$  (bottom) versus age for neutron stars with thermal emission. Data from Table 1 are marked as “H atmosphere fits” and data from Table 2 as “Blackbody fits”.

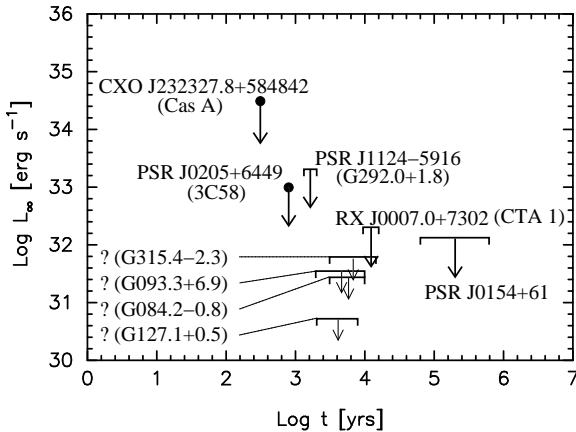


Fig. 2.— Inferred upper limits on thermal luminosity  $L_\infty$ , versus age, for the compact objects listed in Table 3.

nant, the age can also be estimated by the general properties of the remnant and, in the best cases, by association with historical supernovae. We will generically refer to these various alternatives to  $t_{sd}$  as the “kinematic age”  $t_{kin}$ . Both ages, where available, are shown in Tables 1, 2 and 3. The data in these tables show that, in general, there is a large discrepancy between the spin-down age and the kinematic age in cases where both are given. In most cases, the spin-down age is longer, but in the case of the Vela pulsar, it is shorter. Typical discrepancies are of order 3 or larger. For this reason, we have used the kinematic age in Figures 1 and 2 where available, and otherwise have assigned an uncertainty of a factor of 3 in each direction to the spin-down ages.

### 2.3. Distances and Luminosities

The distances are estimated from pulsar dispersion measures, estimated distances to the related supernova remnants, or observations of interstellar absorption to other stars in proximity. In three cases, parallax estimates are available. The details are discussed in Appendix A. Uncertainties in the distances are in many cases rather large. Since the inferred luminosities of the stars are proportional to the square of the assumed distances, it is usually the case that the inferred stellar luminosity has greater relative error bars than the inferred stellar temperature. However, in cases in which the composition of the stellar atmosphere is uncertain, but the distance to the source is accurately known, the inferred stellar luminosity might be more accurately estimated. A consistency check of the measurements of  $T_\infty$ ,  $L_\infty$  and the distance  $d$  is that the relation

$$L_\infty = 4\pi R_\infty^2 \cdot \sigma_{SB} T_\infty^4 \quad (1)$$

should give a radius at infinity  $R_\infty$  comparable to the radius of a neutron star. This is the case for the measurements listed in Table 1, whereas for the measurements based on BB spectral fits listed in Table 2 only 1055-52 has a possibly acceptable  $R_\infty$ , but with very large errors due to the uncertainty in  $d$ . However, BB models are overly simplistic. Non-magnetic heavy-element dominated atmospheres tend to have values of  $R_\infty$  factors of 2 to 3 larger than a BB (Romani 1987), so that essentially all the sources listed in Table 2 satisfy this consistency check. For the objects listed in

Table 3, this consistency test is only marginally possible for J0205+6449 (3C58).

Theoretical cooling calculations also give an effective temperature  $T_e^\infty$  and a luminosity  $L^\infty$  which are related to each other by the equation (see also equation (B9))

$$L^\infty \equiv e^{2\Phi(R)} L(R) = 4\pi R^{\infty 2} \cdot \sigma_{SB} T_e^{\infty 4}, \quad (2)$$

where we have used the superscript  $\infty$  to denote the theoretical values and subscript  $\infty$  for the observed values at infinity in order to emphasize the difference. It is only for a star for which the measured  $T_\infty$  and  $L_\infty$  satisfy equation (2), and for which an accurate measurement of  $d$  exists (implying a small error bar on  $L_\infty$ ), that comparison of cooling curves with data in terms of  $T$  or  $L$  are equivalent. For the stars listed in Table 2 which do not pass the above consistency test, the measured  $T_\infty$  is thus *not* an effective temperature and cannot be directly compared with the calculated  $T_e^\infty$ . In these cases, the luminosity  $L_\infty$  is more representative of thermal emission and should be used for comparison with  $L^\infty$ . For this reason, we have chosen to tabulate luminosities as well as temperatures in Tables 1 and 2, and have plotted both temperature and luminosity in Figure 1. In Table 3, we have reported only upper limits to  $L_\infty$ , which is the quantity that observation can usefully constrain, and plotted them separately in Figure 2.

One feature notable in Figures 1 and 2 is the sizes of the error boxes, particularly in the age dimension. These uncertainties represent an inherent difficulty in using these observations to firmly constrain the details of neutron star cooling. For this reason, instead of attempting to detail properties of the equation of state, superconductivity, and/or neutrino emissivities from the observations, our approach will be to model a reasonably broad range of acceptable physical inputs in order to determine ranges of parameters that might be excluded by the present data.

### 3. INPUT PHYSICS

The standard general relativistic equations determining the structure and thermal evolution of a neutron star are briefly summarized in Appendix B. Given an equation of state (EOS), described in § 3.1, we solve numerically the TOV

equations of hydrostatic equilibrium, and build our stars. The equations of energy conservation, equation (B2), and energy transport, equation (B5), with their corresponding boundary conditions are then solved numerically with a fully general relativistic Henyey-type stellar evolution code specially developed for neutron stars (Page 1989). The required physics input are described in the next section. The outer boundary condition, equation (B6), is implemented in terms of an envelope, described in § 4.

#### 3.1. The Equation of State

The gross properties of a neutron star (such as its mass and radius) and its interior composition (which influences the thermal evolution) chiefly depend on the nature of strong interactions in dense matter. Investigations of dense matter can be conveniently grouped into three broad categories: nonrelativistic potential models, effective field theoretical (EFT) models, and relativistic Dirac-Brueckner-Hartree-Fock (DBHF) models. In addition to nucleons, the presence of softening components such as hyperons, Bose condensates or quark matter, can be incorporated in each of these approaches. Some general attributes, including references and typical compositions, of equations of state (EOS's) in each of these approaches have recently been summarized by Latimer & Prakash (2001).

In this work, we employ four EOS's in the category of nonrelativistic potential models in which only nucleonic degrees of freedom are considered. Two of these are taken from the calculations of the Argonne and Urbana groups. The EOS labeled WFF3, from Wiringa, Fiks & Fabrocini (1988), is based on the variational calculations using UV14+TNI potential and that labeled APR, from Akmal, Pandharipande & Ravenhall (1998), utilizes the AV18 potential plus the UIX potential plus the  $\delta v_b$  boost. APR represents the most complete study to date of Akmal & Pandharipande (1997), in which many-body and special relativistic corrections are progressively incorporated into prior models including that of WFF3.

For isospin symmetric matter, the equilibrium densities of the WFF3 and APR models are  $n_0 = 0.163 \text{ fm}^{-3}$  and  $0.16 \text{ fm}^{-3}$ , respectively, with corresponding compression moduli of 269 MeV and 274 MeV, respectively. In isospin asymmetric

matter, the density dependent symmetry energy  $S(n_b, x)$  is defined by the relation

$$E(n_b, x) = E(n_b, 1/2) + S(n_b, x), \quad (3)$$

where  $E$  is the energy per particle,  $n_b = n_n + n_p$  is the baryon number density, and  $x = n_p/n_b$  is the proton fraction. In practice,  $S(n_b, x)$  can be expanded as

$$S(n_b, x) = S_2(n_b)(1 - 2x)^2 + S_4(n_b)(1 - 2x)^4 \cdots, \quad (4)$$

where the term involving  $S_4$  is generally very small.  $S(n_b, x)$  plays a crucial role in a neutron star's thermal evolution insofar as it determines the equilibrium proton fraction, which in turn determines whether or not the direct Urca process,  $n \rightarrow p + e^- + \bar{\nu}_e$ , is permitted to occur in charge neutral beta-equilibrated matter (Lattimer et al. 1991).

The equilibrium proton fraction is determined from the condition

$$\begin{aligned} \mu_e &= \hat{\mu} = \mu_n - \mu_p = -(\partial E / \partial x) \\ &= 4(1 - 2x)[S_2(n_b) + 2S_4(n_b)(1 - 2x)^2 + \cdots], \end{aligned} \quad (5)$$

where  $\mu_i$  ( $i = e, n, p$ ) are the chemical potentials. For ultrarelativistic and degenerate electrons,  $\mu_e = \hbar c(3\pi^2 n_b x)^{1/3}$ , since due to charge neutrality  $n_e = n_p$  in matter in which the only leptons are electrons.

When the electron Fermi energy is large enough (i.e., greater than the muon mass), it is energetically favorable for the electrons to convert to muons through  $e^- \rightarrow \mu^- + \bar{\nu}_\mu + \nu_e$ . Denoting the muon chemical potential by  $\mu_\mu$ , the chemical equilibrium established by the above process and its inverse is given by  $\mu_\mu = \mu_e$ . At the threshold for muons to appear,  $\mu_\mu = m_\mu c^2 \cong 105$  MeV. Noting that the proton fraction at nuclear density is small, one has the approximate relationship  $4S_2(u)/m_\mu c^2 \sim 1$ , where  $u = n_b/n_0$ . Using a typical value  $S_2(u = 1) \simeq 30$  MeV, one may expect muons to appear roughly at nuclear density  $n_0 = 0.16 \text{ fm}^{-3}$ . Above the threshold density,

$$\mu_e = \hat{\mu} = \mu_\mu = \sqrt{(\hbar c)^2(3\pi^2 n_b x_\mu)^{2/3} + m_\mu^2 c^4}, \quad (6)$$

where  $x_\mu = n_\mu/n_b$  is the muon fraction in matter. The charge neutrality condition now takes the form  $n_e + n_\mu = n_p$ , which, together with the

relation of chemical equilibrium in equation (6), establishes the lepton and proton fractions in matter. The appearance of muons has the consequence that the electron fraction  $x_e = n_e/n_b$  is lower than its value without the presence of muons.

If  $S(n_b, x)$  does not rise sufficiently rapidly with density, the equilibrium proton fraction will remain below a critical value (of order 11% in matter with  $e^-$  only and 14% in matter with both  $e^-$  and  $\mu^-$ ) required for the direct Urca process. The critical proton fraction is determined by requiring simultaneous conservation of energy and momentum among the participating fermions. In this case, cooling occurs via the modified Urca process,  $n + n \rightarrow n + p + e^- + \bar{\nu}_e$ , and several other similar processes (see § 3.5), modulated by effects of possible nucleon superfluidity. Because of the additional fermions involved, the emissivity of the modified Urca process is several orders of magnitude lower than the direct Urca process.

The symmetry energies  $S_2(n_0)$  of the WFF3 and APR models at their respective equilibrium densities  $n_0$  have the values 29.5 MeV and 32.6 MeV, respectively. In the WFF3 model, the symmetry energy  $S_2(n_b)$  rises slowly with density and  $x$  never reaches the critical value for the direct Urca process. However, in the case of the APR model, the direct Urca process becomes possible at  $n_B > 0.78 \text{ fm}^{-3}$ , which corresponds to a neutron star mass of  $M_{cr} = 1.97 M_\odot$ . For this model, we will therefore consider only stars with masses below this threshold.

We also consider two EOS's from the phenomenological non-relativistic potential model of Prakash et al. (1997) which is designed to reproduce the results of more microscopic calculations at zero temperature, and which allows extensions to finite temperature. The EOS's chosen are labeled BPAL21 and BPAL31, which have bulk nuclear matter incompressibilities  $K_s = 180$  or 240 MeV, respectively. In both cases, the symmetry energy, at the empirical symmetric matter equilibrium density of  $n_0 = 0.16 \text{ fm}^{-3}$ , was chosen to be 30 MeV. Furthermore, the potential part of  $S(n_b, x)$  varies approximately as  $\sqrt{n_b/n_0}$  in both cases, which is close to the behavior exhibited in the EOS of APR.

In Figure 3, the symmetry energies (top panel) and corresponding proton fractions (bottom panel) in charge-neutral beta-stable neutron



star matter are shown. In Figure 4, the pressure of neutron star matter is shown as a function of baryon density for the EOS's considered in this work. The differences in the high-density behavior of these two EOS's are largely attributed to differences in the underlying three-body interactions.

The reason why we do not consider EOS's based on effective field-theoretical (EFT) and relativistic Dirac-Brueckner-Hartree-Fock (DBHF) models in this work merits some discussion. In EFT approaches based on the prototype Walecka model, interactions between nucleons are mediated by the exchange of  $\sigma$ -,  $\omega$ -, and  $\rho$ - mesons. At the mean field level, the symmetry energy in this approach is given by (Horowitz & Piekarewicz (2001))

$$S_2(n_b) = \frac{k_F^2}{6\sqrt{k_F^2 + M^{*2}}} + \frac{n_b}{8\left(\frac{g_\rho^2}{m_\rho^2} + 2f(\sigma_0, \omega_0)\right)}, \quad (7)$$

where  $\sigma_0$ ,  $\omega_0$ , and  $\rho_0$  are the mean-field expectation values of the fields,  $g_\sigma$  and  $g_\rho$  are the  $\sigma$ - and  $\rho$ - meson couplings to the nucleon, and  $M^* = M - g_\sigma\sigma_0$  is the nucleon's Dirac effective mass. The quantity  $f(\sigma_0, \omega_0)$  summarizes effects of density dependent nonlinear interactions arising from  $\sigma$ -,  $\omega$ -, and  $\rho$ - mixings and have recently been employed to explore deviations from the linear behavior of the second term with density in the case  $f = 0$ . When the symmetry energy rises linearly with density, the critical proton fraction for the direct Urca process is reached at  $2 - 3 n_0$ , which is well within the central densities of both  $1.4M_\odot$  and maximum mass stars obtained with these EOS's. It is possible, however, to forbid the direct Urca process with a suitable choice of  $f \neq 0$  (Steiner et al. 2004). These cases, however, resemble the potential models considered above.

All DBHF calculations reported thus far in the literature (e.g. M  ther, Prakash & Ainsworth (1987); Engvik et al. (1994)) find that proton fractions favorable for the direct Urca process to occur are reached in stars whose masses are larger than  $\sim 1.3M_\odot$ . Since our intention here is to explore the extent to which model predictions can account for observations without invoking the direct Urca process and its variants involving hyperons, Bose condensation or quarks, we defer a discussion of these models to a separate work.

In Figure 5, we show the mass versus radius and

versus central density curves for the four EOS's chosen. Features of relevance to the discussion of cooling to note are:

- The radii of maximum mass configurations ( $1.7 < M_{max}/M_\odot < 2.2$ ) are confined to the narrow range 9–10 km.
- The radii of  $1.4M_\odot$  stars lie in the narrow range 11 – 12 km.

Significant deviations from such a tight clustering of radii occur only in those cases in which

- normal nucleonic matter is described through the use of EFT or DBHF models. Lattimer & Prakash (2001) showed that the neutron star radius is proportional to the density derivative of the symmetry energy in the vicinity of nuclear matter density. Therefore, in this case, relatively large radii for both  $1.4M_\odot$  and maximum mass configurations occur. Similarly, a relatively large density dependence of the symmetry energy also permits the direct Urca process to occur in this case.
- extreme softening is induced by the presence of additional components such as hyperons, Bose condensates or quarks: In this case, significantly smaller radii are possible. Such components also lead to relatively rapid cooling.

As mentioned earlier, both of these cases fall outside the “Minimal Cooling Scenario” and will be investigated separately.

For completeness, we note that in all four cases considered, the crust-core transition occurs at  $n_b \sim 0.1 \text{ fm}^{-3}$  or equivalently  $\rho \sim 1.6 \times 10^{14} \text{ g cm}^{-3}$ . For the EOS in the crust region, we employ the EOS of Negele & Vautherin (1973) above neutron drip and that of Haensel, Zdunik, & Dobaczewski (1989) below neutron drip.

### 3.2. Nucleon Effective Masses

Under degenerate conditions ( $T \ll \mu$ ) and in the absence of collective excitations close to the Fermi surface, physical quantities such as the specific heat, entropy, and superfluid gaps, and processes such as neutrino emission from particles

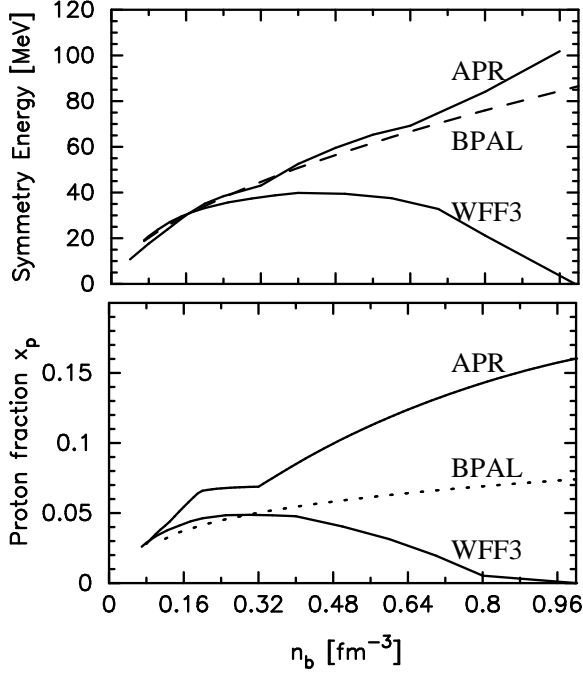


Fig. 3.— Symmetry energy (top panel) and proton fraction (bottom panel) for the four EOS's used in this work.

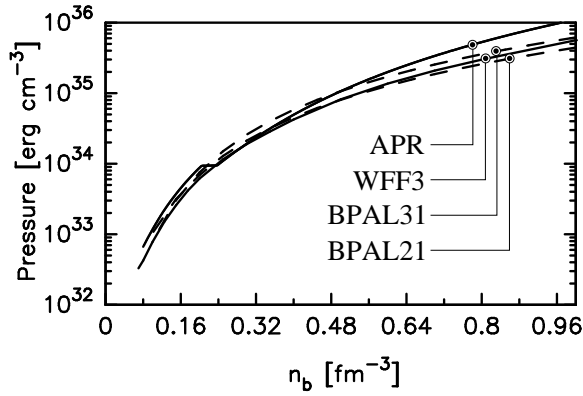


Fig. 4.— Pressure vs baryon density for the four EOS's employed in this work.

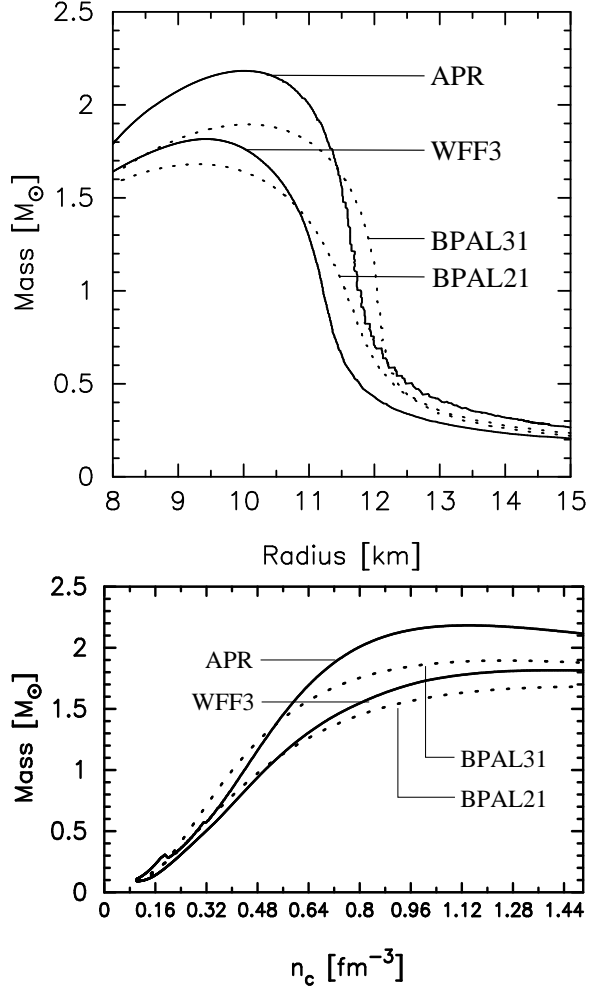


Fig. 5.— Mass versus radius (top panel) and versus central baryon density (bottom panel) for the four EOS's employed in this work.

with energies in the neighborhood of the Fermi energy, depend sensitively on the so-called Landau effective masses of particles. Formally, the Landau effective mass  $m^*$  of any degenerate fermion ( $n$ ,  $p$ ,  $e$ , and  $\mu$  in our case) is defined by

$$m^* \equiv p_F \left[ \frac{\partial e(p)}{\partial p} \Big|_{p=p_F} \right]^{-1}, \quad (8)$$

where  $e(p)$  is the single-particle energy of the particle with momentum  $p$ , and the derivative is evaluated at the Fermi momentum  $p_F$ . For nonrelativistic interacting nucleons, the single particle energies of the neutron and proton can be written as

$$\begin{aligned} e_n(p) &= \frac{p^2}{2m} + U_n(n_b, p) \\ e_p(p) &= \frac{p^2}{2m} + U_p(n_b, p) \end{aligned} \quad (9)$$

where  $m$  is the nucleon mass in vacuum, and  $U_n$  and  $U_p$  are the neutron and proton single-particle momentum-dependent potentials which are obtained by appropriate functional differentiations of the potential energy density.

From the Hamiltonian density in Appendix A of APR, the neutron and proton Landau effective masses are

$$\frac{m^*}{m} = \left[ 1 + \frac{2m}{\hbar^2} (p_3 + zp_5) n_b e^{-p_4 n_b} \right]^{-1} \quad (10)$$

where  $z = (1 - x)$  for neutrons and  $z = x$  for protons, and  $p_3 = 89.8 \text{ MeV fm}^5$ ,  $p_4 = 0.457 \text{ fm}^3$ , and  $p_5 = -59 \text{ MeV fm}^5$ . The solid curves in Figure 7 show the variation of the effective masses with density for both neutrons and protons in charge-neutral beta-stable matter corresponding to the EOS of APR.

To date, single-particle energies for the WFF3 model are available only for symmetric nuclear matter up to  $n_b = 0.5 \text{ fm}^{-3}$  (Wiringa (1988)). Using the parameterization from equation (7) of Wiringa (1988), we find that

$$\frac{m^*}{m} = \left[ 1 - \frac{2m}{\hbar^2 \Lambda^2} \beta \left( 1 + \frac{k_F^2}{\Lambda^2} \right)^{-2} \right]^{-1} \quad (11)$$

where the density-dependent parameters  $\beta$  and  $\Lambda$  are tabulated in Table I of Wiringa (1988). The

filled circles in Figure 7 show the symmetric matter Landau effective masses for this case. Lacking further input, and encouraged by the fact that the APR results for neutron and proton effective masses in beta-stable isospin asymmetric matter bracket the WFF results in isospin symmetric matter, we take the results of the APR model to apply for the WFF model as well. As we will show, our final results are not significantly affected by this approximation.

The neutron and proton Landau effective masses for the BPAL21 and BPAL31 models can be obtained straightforwardly from the single-particle potentials given in Prakash et al. (1997). Explicitly,

$$\begin{aligned} \frac{m^*}{m} &= \left[ 1 - \sum_{i=1,2} (\beta_i + \gamma_i z) u \left[ 1 + \frac{(2zu)^{2/3}}{R_i^2} \right]^{-2} \right]^{-1} \\ \beta_i &= \frac{2(2C_i + 4Z_I)}{5 E_F^0 R_i^2} \quad \gamma_i = \frac{2(C_i - 8Z_I)}{5 E_F^0 R_i^2} \end{aligned} \quad (12)$$

where  $E_F^0$  is the Fermi energy at the equilibrium density  $n_0$  and the parameters  $C_i$ ,  $Z_i$  and  $R_i$  can be found in Tables 1 and 2 of Prakash et al. (1997). The dash dotted curves in Figure 7 show the effective masses for the BPAL models.

The general trends to note in Figure 7 are

- the steady decrease of  $m_n^*$  and  $m_p^*$  with density, and
- $m_n^* > m_p^*$  in charge-neutral beta-stable matter.

It is interesting to observe that there is more spread in the model predictions for  $m_n^*$ , particularly with increasing density, than for  $m_p^*$ .

For noninteracting relativistic particles, such as  $e$  and  $\mu$ , the Landau effective masses are given by

$$m^* c^2 = \sqrt{m^2 c^4 + p_F^2 c^2} \quad (13)$$

where  $m$  denotes the appropriate vacuum mass.

### 3.3. Pairing

The Fermi surface of a degenerate system of fermions, as are  $e$ 's,  $\mu$ 's,  $p$ 's and  $n$ 's in a catalyzed neutron star, becomes unstable in the presence of an attractive interaction between the particles

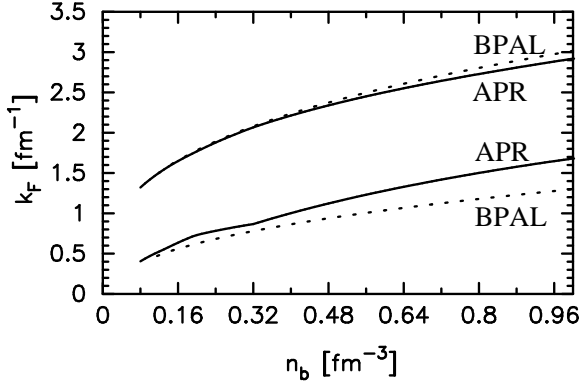


Fig. 6.— Fermi momenta of neutrons (upper curves) and protons (lower curves) versus baryon density for the APR and BPAL EOS's (BPAL21 and BPAL31 give nearly the same values).

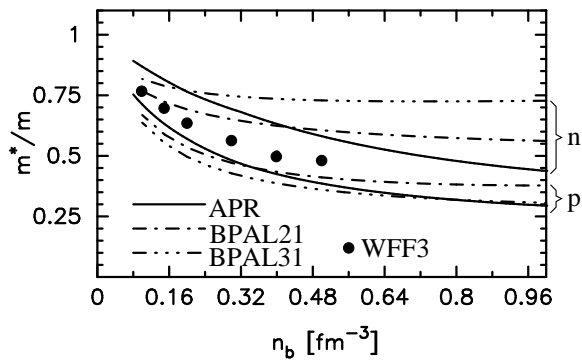


Fig. 7.— Ratio of the Landau effective mass  $m^*$  to the vacuum mass  $m$  for neutrons and protons vs. density for the four EOS's.

whose momenta lie close to the Fermi momentum: this is the Cooper theorem (Cooper 1956). As a result of this instability, the ground state of the system is reorganized with a gap  $\Delta$  in the energy spectrum around the value of the Fermi energy; no particle can have an energy between  $E_F - \Delta$  and  $E_F + \Delta$ .

This instability usually appears as a second order phase transition, the gap acting as the order parameter of the transition which has a corresponding critical temperature  $T_c$ . For  $T > T_c$ , the system behaves as a normal Fermi liquid whereas for  $T \lesssim T_c$  the gap grows in magnitude which results in superfluidity or superconductivity. The precise value of  $T_c$  depends on the nature of the pairing interaction.

There is no obvious attractive interaction between  $e$ 's and/or  $\mu$ 's in a neutron star and thus they are not expected to become paired at temperatures relevant for our concerns here (Baym & Pethick 1975).

For nucleons, the strong interaction provides several channels in which pairing is possible with  $T_c$ 's of order MeV. Nucleon-nucleon scattering data in vacuum indicate that at low momentum pairing should occur through Cooper pairs with zero angular momentum  $L$  in a spin-singlet state,  $^1S_0$ , whereas for larger momenta an  $L = 1$  spin-triplet ( $J = L + S = 2$ ),  $^3P_2$  pairing becomes favorable. Starting from a knowledge of the nucleon-nucleon interaction in vacuum, the difficulty of obtaining reliable values of the gap in a medium is illustrated by considering the result for the solution of the gap equation in the so called *BCS weak coupling approximation* (Bardeen, Cooper & Schrieffer 1957):

$$\Delta \sim E_F e^{-1/VN(0)}, \quad (14)$$

where  $V$  is the in-medium pairing interaction in the corresponding channel and  $N(0) \equiv m^* p_F / \pi^2 \hbar^3$  is the density of states at the Fermi surface. Small variations of  $m^*$  and medium effects on  $V$  affect  $\Delta$  in an exponential manner.

The best-studied case is the  $n$   $^1S_0$  gap in pure neutron matter. The gap appears at densities of order  $n_0$  or lower, where  $m_n^*$  is well determined and the pairing interaction in vacuum for the  $^1S_0$  channel is accurately known. Simple arguments (Pines 1971) show that medium polarization, the

dominant medium effect on  $V$ , should induce a reduction of the  $^1S_0$  gap (Clark et al. 1976) from its value without medium polarization. Much effort has been dedicated to take into account medium polarization at various levels of approximation. With time and improving many-body techniques, the results are beginning to show a convergence for the maximum value of  $T_c$ , which is in the range  $\sim 0.5$  to  $0.7 \times 10^{10}$  K, as can be seen in Figure 8. The density range in which this gap is non-zero is still somewhat uncertain and corresponds to the inner part of the crust and, possibly, the outermost part of the core.

Since the results shown in Figure 8 are for uniform pure neutron matter, they will be altered by the presence of a small fraction of protons in the outer core and the nonuniformity of neutron density due to nuclei (or nuclear clusters) in the inner crust. This latter effect has been studied recently by Barranco et al. (1997) who show that it does not alter significantly the results, at least at the level of accuracy required for the study in the present paper.

The  $p$   $^1S_0$  gap is similar to the  $n$   $^1S_0$  gap and occurs at similar Fermi momenta  $k_F$ , but since protons represent only a small fraction of the nucleons, this translates to high densities which allows the gap to persist in much deeper regions of the core than the  $n$   $^1S_0$  gap. The values of  $T_c$  from several calculations are shown in Figure 9. An essential immediate difference compared to the  $n$   $^1S_0$  gap is that the  $p$   $^1S_0$  gap is much smaller,  $m_p^*$  being smaller for protons than for neutrons (see Figure 7). It should be noted that all calculations shown in this figure have employed values of  $m_p^*$  larger than the values we report in Figure 7. Insofar as the results of Figure 7 for APR are indicative of the likely magnitudes of  $m_p^*$ , the values of  $T_c$  in Figure 9 are likely overestimated, particularly at large  $k_F$ . Moreover, medium polarization effects on  $V$  are much more difficult to take into account for the  $p$   $^1S_0$  gap than for the neutron gap. Such effects are expected to reduce the size of the gap and, to date, only two works have attempted to include them (Niskanen & Sauls 1981; Ainsworth, Wambach & Pines 1991). The estimates of Ainsworth, Wambach & Pines (1991) show that medium polarization reduces the  $^1S_0$  gap roughly by a factor of three in the stellar core. It is important to notice that *all* these calculations

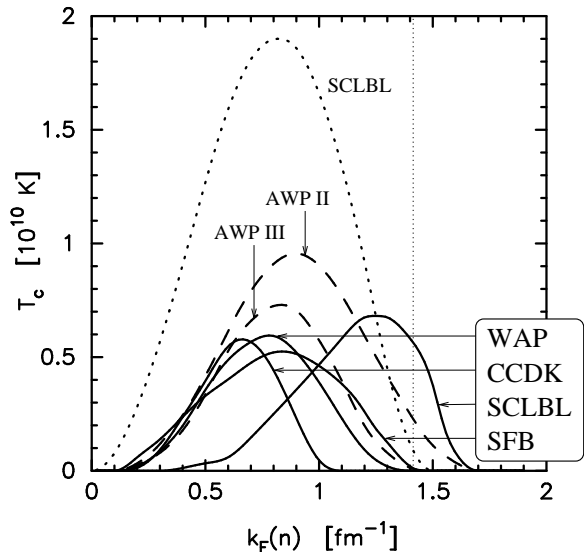


Fig. 8.— Neutron  $^1S_0$  pairing critical temperature  $T_c$  vs neutron Fermi momentum  $k_F$  from the calculations of Ainsworth, Wambach & Pines (1989) (labeled as “AWP II” & “AWP III”: two slightly different results), Wambach, Ainsworth & Pines (1993) (“WAP”), Chen, et al. (1993) (“CCDK”), Shulze et al. (1996) (“SCLBL”), and Schwenk, Friman & Brown (2003) (“SFB”). The dotted curve shows the results of Shulze et al. (1996) in the case where medium polarization is not included. Medium polarization effects reduce the  $^1S_0$  gap by about a factor three. The vertical dotted line shows the location of the crust-core boundary.

find that  $T_c$  vanishes for  $k_F > 1.5 \text{ fm}^{-1}$  and in most cases for  $k_F > 1 \text{ fm}^{-1}$ .

The so-called  $n \ ^3P_2$  gap actually occurs in the  $^3P_2 - ^3F_2$  channel, since the tensor interaction couples channels with  $\delta L = 2$ . This coupling with the  $^3F_2$  channel increases the gap (Takatsuka 1972a). We present an illustrative sample of published  $T_c$  curves in Figure 10. The large differences among these curves points to the inherent difficulty in pinning down the magnitude of this gap. The gap possibly extends to high densities where  $m_n^*$  is uncertain. In addition, the presence of a small fraction of protons has generally been ignored except in the work of Elgarøy et al. (1996), who found a reduction of the gap by a factor  $\sim 3$  when considering neutron-proton matter in  $\beta$ -equilibrium.

A fundamental problem, emphasized recently by Baldo et al. (1998), is that even the best modern models of the nucleon-nucleon interaction (*in vacuum*) fail to reproduce the experimental phase shift in the  $^3P_2$  channel at laboratory energies above 300 MeV (corresponding to the pion-production threshold). Translating this energy into an equivalent density implies that the bare pairing interaction is not understood at densities  $\gtrsim 1.7n_0$ . Moreover, medium polarization effects have not been included in any of the calculations displayed in Figure 10. Estimates of such effects had shown that they should strongly enhance the  $^3P_2 - ^3F_2$  gap (Jackson et al. 1982), but the recent results of Schwenk & Friman (2004) indicate that the medium-induced spin-orbit interaction strongly suppresses this gap. For this reason we will also consider the possibility that the  $n \ ^3P_2$  gap is vanishingly small.

The  $J = 2$  with  $L = 1$  or 3 angular momentum and the tensor coupling make the gap equation a system of coupled integral equations, one for each value of the magnetic quantum number  $m_J$  and the gap is not isotropic:  $\Delta = \Delta(\theta, \phi; T)$ , where  $\theta$  and  $\phi$  are the polar angles of the momentum  $\vec{k}$ . Until recently most works had looked for single component solutions with  $|m_J| = 0, 1$  or 2, but Zverev, Clark & Khodel (2003) have shown that when considering multicomponent solutions there are *at least* 13 distinct phases: for 7 of them  $\Delta(\theta, \phi; T)$  vanishes on the Fermi surface at some values of  $(\theta, \phi)$  whereas the other 6 are nodeless. Nodeless gaps are energetically favored over gaps with nodes, but by a small amount [see, e.g.,

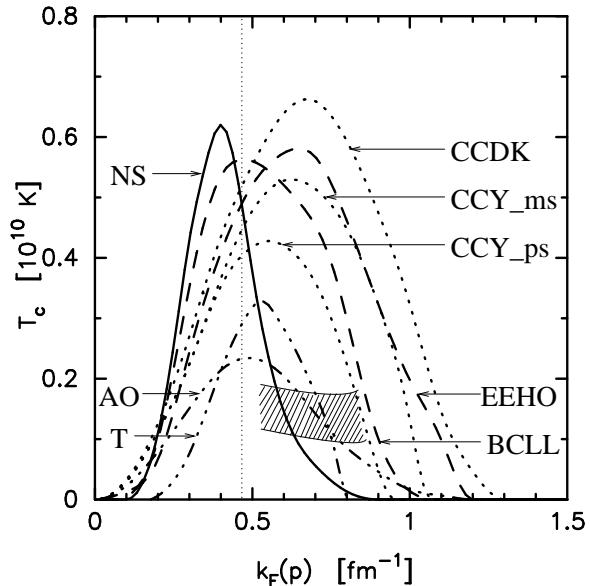


Fig. 9.— Proton  $^1S_0$  pairing critical temperature  $T_c$  vs proton Fermi momentum  $k_F$  from the calculations of Takatsuka (1973) (labeled as “T”), Amundsen & Østgaard (1985a) (“AO”), Chao, Clark & Yang (1972) (“CCY\_ms” & “CCY\_ps”: two slightly different results), Chen, et al. (1993) (“CCDK”), Baldo et al. (1992) (“BCLL”), Elgarøy et al. (1996) (“EEHO”), Niskanen & Sauls (1981) (“NS”). Only the calculation of Niskanen & Sauls (1981) include medium polarization. The shaded region shows the estimates of Ainsworth, Wambach & Pines (1991) of the range of values in which  $T_c$  should lie due to medium polarization. The vertical dotted line shows the location of the crust-core boundary.

Amundsen & Østgaard (1985b)], and may become disfavored in the case of very fast rotation of the star or in the presence of an ultra-strong magnetic field (Muzikar, Sauls, & Serene 1980). We will, in this work, assume that the  ${}^3P_2 - {}^3F_2$  gaps are nodeless, since this maximizes the effect of pairing on cooling and seems energetically favored, and more specifically assume its angular dependence to be  $\Delta(\theta, \phi; T) \propto (1 + 3 \cos^2 \theta)^{1/2}$ , corresponding to the pure  $m_J = 0$  phase.

For both the isotropic  ${}^1S_0$  and the pure  $m_J = 0$  phase of the  ${}^3P_2 - {}^3F_2$  gap, the critical temperature  $T_c$  and the  $T = 0$  gap are related by

$$k_B T_c \approx 0.57 \Delta_0 \quad (15)$$

where  $\Delta_0$  is  $\Delta(T = 0)$  for  ${}^1S_0$  and the angle averaged value of  $\Delta(\theta, \phi; T = 0)^2$  over the Fermi sphere for  ${}^3P_2 - {}^3F_2$  (Baldo et al. 1992). The temperature dependence of  $\Delta$  for these two cases has been calculated and fitted by simple analytical expressions by Levenfish & Yakovlev (1994a).

Once the energy gap  $\Delta$  is given, the quasi-particle energy spectrum near the vicinity of the Fermi surface can be expressed as

$$\begin{aligned} e(\mathbf{k}) &= E_F - \sqrt{\Delta(\mathbf{k})^2 + \eta^2} & \text{for } k < k_F \\ &= E_F + \sqrt{\Delta(\mathbf{k})^2 + \eta^2} & \text{for } k > k_F \end{aligned} \quad (16)$$

where the quantity  $\eta$  is given by

$$\begin{aligned} \eta &= \frac{k^2}{2m^*} - \frac{k_F^2}{2m^*} \\ &\cong \left( \frac{k_F}{m^*} \right) \cdot (k - k_F) \equiv v_F \cdot (k - k_F) \end{aligned} \quad (17)$$

The effect of this change in the quasi-particle spectrum is discussed below in § 3.4 and § 3.5.

Finally, it is instructive to consider  $T_c$  for the  $p$   ${}^1S_0$  gap and the  $n$   ${}^3P_2 - {}^3F_2$  gap in terms of density and also in terms of the volume in the stellar core, once an EOS and a stellar mass has been chosen. (This is presented for a few cases in Figures 20 and 21 in a  $1.4 M_\odot$  star built with the APR EOS.) The  $p$   ${}^1S_0$  gap vanishes or is very small in the inner core for most calculations whereas the  $n$   ${}^3P_2 - {}^3F_2$  gap is more likely to reach the stellar center with high values.

### 3.4. The Specific Heat

The total specific heat (per unit volume) at constant volume,  $c_v$ , receives contributions from all of

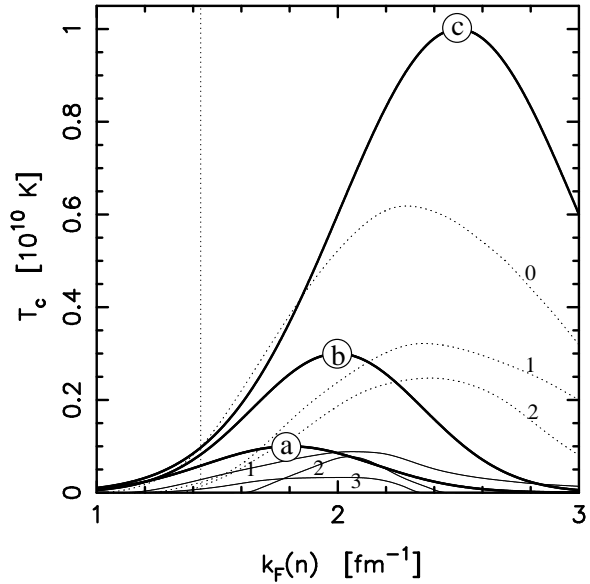


Fig. 10.— Neutron  ${}^3P_2 - {}^3F_2$  pairing critical temperature  $T_c$  vs neutron Fermi momentum  $k_F$ . The three thin continuous lines show the results of: (1) Amundsen & Østgaard (1985b), (2) Takatsuka (1972b), and (3) Elgarøy et al. (1996). The three dotted lines show results obtained assuming  $m_n^* = m_n$  to illustrate the strong reduction due to small  $m_n^*$ : (0) Hoffberg et al. (1970), (1) Amundsen & Østgaard (1985b), and (2) Takatsuka (1972b). The three thick continuous lines, (a), (b), and (c), bracket the results of Baldo et al. (1998). The vertical dotted line shows the location of the crust-core boundary.

the constituents inside the star. In the homogeneous phase above nuclear density,

$$c_v = \sum_{i=e^-, \mu^-, n, p} c_{i,v} \quad (18)$$

For a given species of unpaired spin  $\frac{1}{2}$  fermions,  $c_v$  is given by

$$\begin{aligned} c_v &= \frac{1}{n_b} \frac{\partial \epsilon}{\partial T} \\ &= 2 \int \frac{d^3 k}{(2\pi)^3} (e - \mu) \frac{\partial f}{\partial T} - T \frac{\left( 2 \int \frac{d^3 k}{(2\pi)^3} \frac{\partial f}{\partial T} \right)^2}{2 \int \frac{d^3 k}{(2\pi)^3} \frac{\partial f}{\partial \mu}} \end{aligned} \quad (19)$$

where  $e(k)$  is the single-particle spectrum,  $f$  is the Fermi-Dirac distribution function, and  $\mu$  and  $T$  are the chemical potential and temperature, respectively. Under the degenerate conditions of interest here,  $T \ll \mu$ , the contribution from the second term above can be safely neglected with the result

$$c_{i,v} = N_i(0) \frac{\pi^2}{3} k_B^2 T = \frac{m_i^* n_i}{p_{i,F}^2} \pi^2 k_B^2 T \quad (20)$$

In writing the rightmost relation above, the density of states at the Fermi surface  $N_i(0)$  has been expressed in terms of the Landau effective mass  $m_i^*$  (see equation (8)) through the relations

$$N_i(0) = \frac{3n_i}{k_F v_F}, \quad v_F = \left. \frac{\partial e}{\partial k} \right|_{k_F} \quad (21)$$

where  $v_F$  denotes the velocity at the Fermi surface.

The effect of pairing interactions on the specific heat depends on the disposition of  $T$  with respect to  $T_c$ . When  $T$  reaches  $T_c$ , there is a sharp increase in the specific heat due to the large fluctuations characteristic of a second order phase transition. Subsequently, when  $T \ll T_c$ , a Boltzmann-like suppression occurs due to the presence of a gap in the energy spectrum, equation (16). In practice, these effects are taken into account by using control functions that would multiply the unpaired values of  $c_v$ ; these functions have been calculated for nucleon pairing in both the  $^1S_0$  and  $^3P_2$  channels by Levenfish & Yakovlev (1994a) and are displayed in the upper panel of Figure 13.

The cumulative contributions to  $c_v$  are presented in Figure 11. Once a nucleonic component

becomes paired, its contribution will ultimately be suppressed when  $T \ll T_c$ , but in all cases the lepton contribution will always remain. For different temperatures the various contributions all scale as  $T$  in the absence of pairing and their relative importance hence remains the same as illustrated in this figure.

The suppression by pairing is illustrated in Figure 12 for the case of neutrons at various temperatures beginning with  $10^9$  K as in Figure 11. The results in this figure, in agreement with those in Figure 13, show that beyond the initial strong enhancement at  $T \lesssim T_c$ ,  $c_v$  will be almost completely suppressed only when  $T < 0.1$  to  $0.2 \times T_c$  everywhere within the core.

In the crustal region, contributions to the specific heat arise from the neutron gas in the inner crust, the degenerate electron gas and the nuclear lattice. The contribution of the neutron gas is strongly suppressed by the  $n \ ^1S_0$  gap. The specific heat of the crust is smaller than that of the leptons in the core and is hence not very important, but included in all our calculations.

### 3.5. Neutrino Emissivities

Until the time that photon emission takes over the cooling of the star, the thermal energy of the star is lost from both the crustal layers and the core of the star chiefly by neutrino emission. The various neutrino emission processes that are included in our study are summarized below.

In the crust of the star, we include neutrino pair emission from plasmons according to Haft, Raffelt & Weiss (1994), or, from the practically equivalent results of Itoh et al. (1996), and from electron-ion bremsstrahlung according to Kaminker et al. (1999). These two processes are not affected by nucleon pairing. We also consider neutrino pair emission from neutron-neutron bremsstrahlung and its suppression by neutron pairing. The treatment of pairing suppressions is outlined below in the context of similar suppressions in the core. In addition, we consider neutrino pair emissions from the formation and breaking of  $n \ ^1S_0$  Cooper pairs, also described further below. In the presence of a magnetic field, synchrotron neutrino pair emission from electrons also occurs (Bezchastnov et al. 1997), but contributions from this process are negligible. Photo-neutrino emission and neutrino



pairs from  $e^+e^-$  pair annihilation are effective only at low density and high temperature and are not relevant here.

In the core of the star, we include (1) the modified Urca processes and the similar nucleon bremsstrahlung processes with their corresponding suppressions by nucleon pairing, and (2) neutrino pair emission from the formation and breaking of Cooper pairs. The emissivity from the neutron branch of the modified Urca process

$$\begin{aligned} n + n' &\rightarrow p + n' + l + \bar{\nu}_l \\ p + n' + l &\rightarrow n + n' + \nu_l \end{aligned} \quad (22)$$

where  $l$  is either an electron or a muon and  $\nu_l$  or  $\bar{\nu}_l$  is the associated neutrino or antineutrino, is taken from Friman & Maxwell (1979) and Yakovlev & Levenfish (1995). Explicitly,

$$\begin{aligned} q_\nu^{\text{Murca n}} &= 8.55 \times 10^{21} \left( \frac{m_n^*}{m_n} \right)^3 \left( \frac{m_p^*}{m_p} \right) \\ &\left[ \left( \frac{k_{Fe}}{k_{F0}} \right) + \left( \frac{k_{F\mu}}{k_{F0}} \right) \right] \alpha_n \beta_n \left( \frac{T}{10^9 \text{ K}} \right)^8, \end{aligned} \quad (23)$$

where  $k_{F0} = 1.68 \text{ fm}^{-1}$  is a fiducial normalization factor. The emissivity from the proton branch of the modified Urca process

$$\begin{aligned} n + p' &\rightarrow p + p' + l + \bar{\nu}_l \\ p + p' + l &\rightarrow n + p' + \nu_l \end{aligned} \quad (24)$$

is taken from Yakovlev & Levenfish (1995) in the form

$$\begin{aligned} q_\nu^{\text{Murca p}} &= 8.55 \times 10^{21} \left( \frac{m_n^*}{m_n} \right) \left( \frac{m_p^*}{m_p} \right)^3 \\ &\left[ \left( \frac{k_{Fe}}{k_{F0}} \right) \left( 1 - \frac{k_{Fe}}{4k_{Fp}} \right) + \left( \frac{k_{F\mu}}{k_{F0}} \right) \left( 1 - \frac{k_{Fe}}{4k_{Fp}} \right) \right] \\ &\alpha_p \beta_p \left( \frac{T}{10^9 \text{ K}} \right)^8. \end{aligned} \quad (25)$$

In equations (23) and (25), the coefficients  $\alpha_n$ ,  $\alpha_p$ ,  $\beta_n$ , and  $\beta_p$  are of order unity and describe corrections due to the momentum transfer dependence of the matrix element in the Born approximation ( $\alpha_{n,p}$ ) and due to non-Born corrections and strong interaction effects beyond the one pion exchange plus Landau coefficients ( $\beta_{n,p}$ ) (Friman & Maxwell 1979; Yakovlev & Levenfish 1995). To be specific, following Yakovlev & Levenfish (1995) we use

$$\begin{aligned} \alpha_n = \alpha_p &= 1.76 - 0.63 \left( \frac{k_{F0}}{k_{Fn}} \right)^2 \\ \beta_n = \beta_p &= 0.68. \end{aligned} \quad (26)$$

In addition to the above two charged current modified Urca processes, three neutral current bremsstrahlung processes

$$\begin{aligned} n + n' &\rightarrow n + n' + \nu_l + \bar{\nu}_l \\ n + p' &\rightarrow n + p' + \nu_l + \bar{\nu}_l \\ p + p' &\rightarrow p + p' + \nu_l + \bar{\nu}_l, \end{aligned} \quad (27)$$

where the pairs  $\nu_l \bar{\nu}_l$  can be an  $e$ ,  $\mu$  or  $\tau$  neutrino pair, also contribute. Their emissivities are (Friman & Maxwell 1979; Yakovlev & Levenfish 1995)

$$\begin{aligned} q_\nu^{\text{Brem nn}} &= 3 \times 7.4 \times 10^{19} \left( \frac{m_n^*}{m_n} \right)^4 \\ &\left( \frac{k_{Fn}}{k_{F0}} \right) \alpha_{nn} \beta_{nn} \left( \frac{T}{10^9 \text{ K}} \right)^8, \end{aligned} \quad (28)$$

$$\begin{aligned} q_\nu^{\text{Brem np}} &= 3 \times 1.5 \times 10^{20} \left( \frac{m_n^*}{m_n} \right)^2 \left( \frac{m_p^*}{m_p} \right)^2 \\ &\left( \frac{k_{Fp}}{k_{F0}} \right) \alpha_{np} \beta_{np} \left( \frac{T}{10^9 \text{ K}} \right)^8, \end{aligned} \quad (29)$$

and

$$\begin{aligned} q_\nu^{\text{Brem pp}} &= 3 \times 7.4 \times 10^{19} \left( \frac{m_p^*}{m_p} \right)^4 \\ &\left( \frac{k_{Fp}}{k_{F0}} \right) \alpha_{pp} \beta_{pp} \left( \frac{T}{10^9 \text{ K}} \right)^8, \end{aligned} \quad (30)$$

where the  $\alpha$ 's and  $\beta$ 's are corrections of order unity for which we use (Yakovlev & Levenfish 1995)

$$\begin{aligned} \alpha_{nn} &= 0.59 & \beta_{nn} &= 0.56 \\ \alpha_{np} &= 1.06 & \beta_{np} &= 0.66 \\ \alpha_{pp} &= 0.11 & \beta_{pp} &= 0.70. \end{aligned}$$

It is important to note that the emissivities of the modified Urca and bremsstrahlung processes have not been accurately calculated, particularly at the highest densities reached in the center of the stars we are considering. Voskresensky & Senatorov (1986) have proposed that when the density approaches the critical density for the onset of charged pion condensation, the softening of the pion mode induces a strong increase in the above emissivities. Since this approach assumes the occurrence of charged pion condensation, we will not consider it here as part of the minimal scenario. Nevertheless, less dramatic medium effects

are certainly at work. Recently, Hanhart, Phillips & Reddy (2001); Van Dalen, Dieperink & Tjon (2003); Schwenk, Jaikumar & Gale (2004) have revisited the bremsstrahlung processes, including hadronic polarization up to the two loop level, and found a reduction of the rates by a factor of about 4 at saturation density. In view of this, we will at first take equations (23), (25), (28), (29), and (30), with the quoted  $\alpha$ 's and  $\beta$ 's at face value, but will, in addition, consider the effects of “cranking up” or “down” all modified Urca and bremsstrahlung emissivities by a significant factor in § 5.6.

Once the temperature  $T$  reaches the pairing critical temperature  $T_c$  of either the neutrons or protons in a given layer of the star, the corresponding neutrino emission process becomes suppressed by the development of an energy gap  $\Delta(T)$  in the single particle excitation spectrum (see equation (16)). Similarly to what happens for the specific heat, the neutrino emissivities are suppressed by factors which vary approximately like  $\exp(-\Delta(T)/k_B T)$ . In our calculations, we employ the accurate calculations of these various control functions including pre-exponential factors (see Yakovlev & Levenfish (1995) for details) for the two modified Urca processes and the three bremsstrahlung processes, in the presence of  $n\ ^1S_0$  or  $^3P_2$  pairing and/or  $p\ ^1S_0$  pairing. Two representative examples, for the neutron branch of the modified Urca process, are plotted in the central panel of Figure 13: for this specific case neutron pairing has a much stronger effect than proton pairing since three neutrons, but only one proton, participate in the reaction.

As the temperature begins to approach  $T_c$ , new channels for neutrino emission through the continuous formation and breaking of Cooper pairs (Flowers, Ruderman & Sutherland 1976; Voskresensky & Senatorov 1987) begin to become operative. We take emissivities from these “Pair Breaking and Formation” or PBF processes as (Yakovlev & Levenfish 1995)

$$q_\nu^{p\ ^1S_0} = 2.6 \times 10^{21} \left( \frac{n_b}{n_0} \right)^{1/3} \left( \frac{m_p^*}{m_p} \right) \times \tilde{F}_{1S_0}(T/T_c) \left( \frac{T}{10^9 \text{K}} \right)^7 \quad (31)$$

for  $p\ ^1S_0$  pairing,

$$q_\nu^{n\ ^1S_0} = 1.0 \times 10^{22} \left( \frac{n_b}{n_0} \right)^{1/3} \left( \frac{m_n^*}{m_n} \right) \times \tilde{F}_{1S_0}(T/T_c) \left( \frac{T}{10^9 \text{K}} \right)^7 \quad (32)$$

for  $n\ ^1S_0$  pairing, and

$$q_\nu^{n\ ^3P_2} = 8.6 \times 10^{21} \left( \frac{n_b}{n_0} \right)^{1/3} \left( \frac{m_n^*}{m_n} \right) \times \tilde{F}_{3P_2}(T/T_c) \left( \frac{T}{10^9 \text{K}} \right)^7 \quad (33)$$

for  $n\ ^3P_2$  pairing, assuming again that pairing in this last case occurs in the  $m_J = 0$  phase. The control functions  $\tilde{F}_{1S_0}(T/T_c)$  and  $\tilde{F}_{3P_2}(T/T_c)$  are shown in the lower panel of Figure 13 and give the dependence on  $T_c$ . These PBF processes can be regarded as  $nn$  or  $pp$  bremsstrahlung processes with a strong correlation in the initial state in the case of the breaking of a Cooper pair, or in the final state in the case of the formation of a Cooper pair, and exemplify an extreme case of medium correction to the bremsstrahlung processes. Their efficiencies are similar to those of the bremsstrahlung processes of equations (28), (29), and (30). However, they are less sensitive to the values of the nucleon effective masses because they are proportional to  $m^*$  instead of  $m^{*4}$ . Furthermore, the  $T^7$  dependence of the PBF processes, compared to the  $T^8$  dependence of the bremsstrahlung processes, allows the PBF processes to eventually dominate the total neutrino luminosity. The precise value of  $T_c$  for the neutron and/or proton pairing determines when this dominance occurs, as will become apparent in § 5.4. The form of the control functions (Figure 13) show clearly that the PBF process turns on when  $T$  reaches  $T_c$ , increases its efficiency as  $T$  decreases, and becomes exponentially suppressed when the gap approaches its maximum size  $\Delta(0)$  when  $T \lesssim 0.2T_c$ .

#### 4. THE NEUTRON STAR ENVELOPE

It is customary to separate cooling models into the *interior* and the *envelope*, the latter being the upper layer in which a strong temperature gradient exists whereas the interior designates everything inside which becomes isothermal within a few years after the birth of the neutron star.

Precisely, the envelope can be defined as the layer extending from the *photosphere*, the uppermost layer where the emitted spectrum is determined, down to a boundary density  $\rho_b$  such that the luminosity in the envelope is equal to the total surface luminosity of the star,  $L(r) = L(R)$ . The thermal relaxation time scale of the envelope is much shorter than the cooling time scale of the interior so that it can be treated separately as a layer constantly in a stationary state. Equation (B2) therefore implies that the neutrino emission is negligible in the envelope. Since the thickness of the envelope is of the order one hundred meters or less, the envelope can be treated in the plane parallel approximation. Within these approximations, integration of the heat transport and hydrostatic equilibrium equations gives a relationship between the temperature at the bottom of the envelope,  $T_b$ , and the flux  $F$  going through it, or, equivalently, a relationship between the effective temperature  $T_e$  and  $F$ :  $F \equiv \sigma_{SB} T_e^4$ . This relationship is commonly termed as the “ $T_e - T_b$  relationship”.

Detailed numerical calculations along this line were presented by Gundmundsson, Pethick & Epstein (1982, 1983) and an analytical approximation to these results was provided by Hernquist & Applegate (1984), who assumed that the chemical composition of matter corresponds to that in beta-equilibrium. Gundmundsson, Pethick & Epstein (1982) found a simple analytical relationship

$$T_e = 0.87 \times 10^6 (g_{s14})^{1/4} (T_b/10^8 \text{K})^{0.55}, \quad (34)$$

where  $g_{s14}$  is surface gravity  $g_s$  measured in  $10^{14}$  cgs units. (As a rule of thumb, this gives  $T_e \propto T_b^{1/2}$  and  $T_e \sim 10^6$  K when  $T_b \sim 10^8$  K.) This equation illustrates the fact that the dependence of the envelope structure on  $M$  and  $R$  is entirely contained in  $g_s$  and that  $T_e/g_{s14}^{1/4}$  is independent of  $M$  and  $R$ . This allows us to use “generic” envelope models and glue them to the upper layer of any stellar model.

### The Sensitivity Strip: Effects of Chemical Composition and Magnetic Fields

The most important finding of Gundmundsson, Pethick & Epstein (1982, 1983) is that the  $T_e - T_b$  relationship is mostly determined by the value of the thermal conductivity  $\lambda$  in a thin layer in which ions are in the liquid phase and where  $\lambda$

is dominated by electron conduction. This layer was thus called the “sensitivity strip” in the  $\rho - T$  plane. The sensitivity strip is located at lower densities for lower temperatures and spans about one and a half order of magnitude in density depth.

The presence of light elements (e.g., H, He, C or O) in the envelope can significantly affect the  $T_e - T_b$  relationship if the sensitivity strip is populated by these elements (Chabrier, Potekhin & Yakovlev 1997). Lighter elements will burn into heavier ones in the thermonuclear regime at high enough  $T$  and in the pycnonuclear regime at high enough  $\rho$ , but conditions in the envelope are usually such that H may be present up to densities  $\sim 10^7$  gm cm $^{-3}$ , He up to  $\sim 10^9$  gm cm $^{-3}$  and C up to  $\sim 10^{10}$  gm cm $^{-3}$ . The critical temperatures for thermonuclear burning and densities for pycnonuclear burning are well within the sensitivity strip and one can thus expect a strong effect of light element presence on the  $T_b - T_e$  relationship. This problem was studied in detail by Chabrier, Potekhin & Yakovlev (1997) and Potekhin, Chabrier & Yakovlev (1997), who performed numerical calculations of envelope structure with a pure iron plus catalyzed matter chemical composition and with various amounts of light elements. These authors found that the presence of light elements can significantly raise the surface temperature  $T_s$  for a given  $T_b$  if they are present in sufficient amounts. The larger the amount of light elements present, the higher the temperature at which their effect will be felt due to the temperature dependence of the location of the sensitivity strip. But at very high temperatures, the light elements have practically no effect because they cannot penetrate deep enough. The resulting  $T_e^\infty - T_b$  relationships for various amounts of light elements are shown in Figure 14.

The presence of a magnetic field can also affect the structure of the envelope (Greenstein & Hartke 1983). The effect is to enhance heat transport along the field and inhibit transport along directions perpendicular to the field. This results in a nonuniform surface temperature distribution, with a very cold region in which the field is almost tangential to the surface as, e.g., around the magnetic equator for a dipolar field, and a corresponding modification of the  $T_e^\infty - T_b$  relationship (Page 1995). However, the overall effect is not very large, but is somewhat sensitive to the pres-

ence of strongly nondipolar surface fields (Page & Sarmiento 1996). For a field of the order of  $10^{11}$  -  $10^{12}$  G, one obtains a slight reduction of  $T_e^\infty$  compared to the field-free case, whereas for a higher field  $T_e^\infty$  begins to be enhanced. The enhancement of  $T_e^\infty$  is, however, much smaller than what is obtained by the presence of light elements (Potekhin et al. 2003). Moreover, there are possible instabilities due to the non-uniformity of the temperature (Urpin 2004) which have not yet been taken into account in magnetized envelope calculations and may somewhat affect these results, but we do not expect significant changes. Hence, the important case for our purpose would be the maximal reduction of  $T_e^\infty$  obtained for a pure heavy element envelope at  $B = 10^{11}$  G, which is illustrated in Figure 14.

One must finally mention that our calculations are based on the assumption of spherical symmetry in the interior and that the only asymmetries considered, due to the presence of a magnetic field, are within the envelope and hence included into this outer boundary condition. However, this assumption is questionable in some magnetic field configurations where the field is confined to the stellar crust. As shown by Geppert, Kuecker & Page (2004), the crust is highly non-isothermal in such cases and this can affect the thermal evolution because the resulting photon luminosity is lowered compared to the isothermal crust case.

## 5. A GENERAL STUDY OF NEUTRON STAR COOLING WITHIN THE “MINIMAL SCENARIO”

In this section, we will consider the individual effects of the chief physical ingredients which enter into the modeling of the cooling of an isolated neutron star. Our purpose here is twofold:

(1) to determine the sensitivity of results to uncertainties in input physics in order to obtain a broad range of predictions which, we hope, encompasses all possible variations within the minimal cooling scenario; and,

(2) to provide us with the means to identify the types of models that will result in the coldest possible neutron stars within this paradigm.

Theoretical refutations of the critical physical

ingredients needed for these coldest models could allow us to raise the temperature predictions and possibly provide more, or stronger, evidence for “enhanced cooling”. The task of identifying the minimally cooling coldest star will be taken up in § 6. An object colder than such a star could be considered as evidence for the presence of physics beyond the minimal paradigm.

All results in this section use stars built using the APR EOS, except for § 5.8 where the effects of the EOS are studied for a star of  $1.4 M_\odot$  and for § 5.7 where effects of the stellar mass are studied.

### 5.1. Neutrino vs. Photon Cooling Eras and the Effect of the Envelope

The basic features of the thermal evolution of a neutron star can be easily understood by considering the global thermal energy balance of the star

$$\frac{dE_{\text{th}}}{dt} \equiv C_V \frac{dT}{dt} = -L_\nu - L_\gamma, \quad (35)$$

where  $E_{\text{th}}$  is the total thermal energy content of the star and  $C_V$  its total specific heat. This equation is accurate when the star is isothermal, which is the case for ages larger than a few decades. Since the dominant neutrino processes all have a  $T^8$  temperature dependence, the neutrino luminosity can be expressed as

$$L_\nu = NT^8. \quad (36)$$

Furthermore, most of the specific heat comes from the degenerate fermions in the core for which

$$C_V = CT \quad (37)$$

in the absence of pairing interactions. The photon luminosity can be written as

$$L_\gamma \equiv 4\pi R^2 \sigma_{SB} T_e^4 = ST^{2+4\alpha} \quad (38)$$

where  $T_e$ , the effective temperature, is converted into the internal temperature  $T$  through an envelope model with a power-law dependence:  $T_e \propto T^{0.5+\alpha}$  with  $\alpha \ll 1$  (see equation (34) and Figure 14). Equation (35) is easily integrated in the dominantly neutrino and photon cooling eras.

(1) The *neutrino cooling era* ( $L_\nu \gg L_\gamma$ ): In this case,

$$t = \frac{C}{6N} \left( \frac{1}{T^6} - \frac{1}{T_0^6} \right) \quad (39)$$

where  $T_0$  is the initial temperature at time  $t_0 \equiv 0$ . For  $T \ll T_0$ , this gives

$$T = \left( \frac{C}{6N} \right)^{\frac{1}{6}} t^{-\frac{1}{6}} \quad \text{and} \quad T_e \sim t^{-\frac{1}{12}}. \quad (40)$$

The very small exponent in the  $T_e$  evolution during neutrino cooling is a direct consequence of the strong temperature dependence of  $L_\nu$ .

(2) The *photon cooling era* ( $L_\gamma \gg L_\nu$ ): In this case,

$$t = t_1 + \frac{C}{4\alpha S} \left( \frac{1}{T^{4\alpha}} - \frac{1}{T_1^{4\alpha}} \right) \quad (41)$$

where  $T_1$  is the temperature at time  $t_1$ . When  $t \gg t_1$  and  $T \ll T_1$ , we have

$$T = \left( \frac{C}{4\alpha S} \right)^{\frac{1}{4\alpha}} t^{-\frac{1}{4\alpha}} \quad \text{and} \quad T_e \sim t^{-\frac{1}{8\alpha}}. \quad (42)$$

Since  $\alpha \ll 1$ , we see that, during the photon cooling era, the evolution is very sensitive to the nature of the envelope, i.e.,  $\alpha$  and  $S$ , and to changes in the specific heat, as induced by nucleon pairing.

Figure 15 shows the evolution of  $T_e^\infty$ ,  $T_{\text{center}}^\infty$ ,  $L_\gamma^\infty$ , and  $L_\nu^\infty$  in a simplified model in which no pairing has been included, but two extreme cases of envelope chemical composition, iron-like elements and light elements, are considered. The  $L_\gamma^\infty$  curves of panel C are analogous to the  $T_e^\infty$  curves of panel A, since  $L_\gamma^\infty = 4\pi R_\infty^2 \sigma_{SB} T_e^{\infty 4}$ . For both envelope models the  $T_e^\infty$  vs.  $t$  and  $T_{\text{center}}^\infty$  vs.  $t$  curves follow power laws (i.e., straight lines on a log-log plot) in both the neutrino cooling and photon cooling eras. For  $t \lesssim 10^4$  yrs, both models have the same  $T_{\text{center}}^\infty$  because the envelopes do not contribute to energy loss, neither through neutrino emission (due to their low density and very small mass) nor through photon emission (since  $L_\gamma^\infty \ll L_\nu^\infty$ ). At these times, the model with a light element envelope, however, has a higher  $T_e^\infty$ , and thus  $L_\gamma^\infty$ , due to the more efficient transport of heat in this envelope and will consequently shift from neutrino to photon cooling at a much earlier time. This trend will not be modified by the inclusion of more realistic physics. During the neutrino cooling era,  $T_e^\infty$  simply follows the evolution of the interior temperature and models with light element envelopes appear hotter to an external observer than models with an iron-like envelope, but

they enter the photon cooling era sooner and subsequently cool much faster. Neutron stars with lesser amounts of light elements in the envelope will cool intermediately between the extremes of light-element and heavy-element dominated atmospheres, as displayed in Figure 16.

## 5.2. Time Evolving Envelopes

We consider here the possibility of time evolution of the chemical composition of the envelope. We assume that the mass of the envelope consisting of light elements decays with time as

$$\Delta M_L(t) = e^{-t/\tau} \Delta M_L(0) \quad (43)$$

where  $\Delta M_L(0)$  is the initial mass in light elements. This decay could be due to the pulsar mechanism which injects light elements into the magnetosphere or due to nuclear reactions which convert these elements into heavy ones (Chang & Bildsten 2003a,b). One can expect from this that the star will shift from a cooling trajectory corresponding to a light element envelope toward a trajectory with heavy elements envelope as  $\Delta M_L$  decreases. Figure 17 illustrates this evolution and shows that this shift happens in a short time in the case of an exponential mass reduction. This fast evolution is in agreement with the  $T_e - T_b$  relationships shown in Figure 14 where one sees  $T_e$  changing from the light element case to the heavy element one within a small range of variation of  $\Delta M_L$ , at a value of  $T_b$  depending strongly on  $\Delta M_L$ .

## 5.3. Basic Effects of Pairing

In this subsection, we briefly illustrate the first two significant effects of pairing, suppressions of  $q_\nu$  and  $c_\nu$ . The third effect, neutrino emission through the PBF process is studied in the next section. The continuous lines in Figure 18 compare thermal evolutions of the same neutron star with and without nucleon pairing (the gaps have been chosen so as to maximize effects of suppression). The results are very natural: during the neutrino cooling era the paired star cools more slowly than the unpaired one since its neutrino luminosity  $L_\nu$  is severely suppressed whereas during the photon cooling era it cools faster due to its much reduced specific heat. During the neutrino cooling era, the suppression of  $c_\nu$  is present, but its effect is not so dramatic for three reasons:

(1) the lepton contribution to  $C_V$  is not suppressed, whereas  $L_\nu$  is reduced by many orders of magnitude as only the very inefficient electron-ion bremsstrahlung process in the crust is not suppressed,

(2) when  $T$  is not very much less than  $T_c$ , as is partially the case in this example during the neutrino cooling era, the suppression of  $c_\nu$  is preceded by a phase of enhancement (see, e.g., Figure 12), and

(3) the cooling curve has a relatively small slope when  $T \sim T_0$ . From equation (39), and as represented schematically in Figure 19, one sees that the shift to the  $T \propto t^{-1/6}$  power law occurs at a time  $t_{0-\nu}$  determined by the ratio  $C/6N$ . This ratio is increased by pairing and results in a delayed shift, but this amounts to an horizontal translation of the cooling curve and hence shows no spectacular effect. In contradistinction, during the photon cooling era, the shift in the transition time  $t_{\nu-\gamma}$  from neutrino to photon cooling (this occurs earlier with pairing than without pairing due to the smaller value of  $C/4\alpha S$  in equation (40)) acts on a power law evolution with large slope.

However, the neutrino emission by the PBF process (artificially turned off in this example) alters significantly these simple results as can be seen from the dotted line in Figure 18, and is described below.

#### 5.4. The PBF Neutrino Process

We consider here in detail the effect of the PBF neutrino process. Given the strong  $T^7 F(T/\Delta)$  temperature dependence and the density dependence of  $\Delta$ , the overall effect can only be assessed by complete calculations presented here and in § 7.

As a first step, we consider separately the temperature dependence of the luminosities due to the  $n^3P_2$  and  $p^1S_0$  gaps in the core of a  $1.4 M_\odot$  star built with the EOS of APR. Results for four different  $n^3P_2$  gaps are shown in Figure 20. The lower panel shows the  $T_c$  profiles of these four gaps as a function of the volume of the core (left hand scale) and the density (right hand scale). A vertical line in this panel, which corresponds to an isothermal core, allows one to visualize the amount

of the core's volume which is paired. The upper panel shows the corresponding PBF neutrino luminosity  $L_\nu^{PBF}$ . Also plotted are the surface photon luminosity corresponding to an iron-like envelope (dotted line) and the total neutrino luminosity from the modified Urca and bremsstrahlung processes *without* pairing suppression. Notice that when  $T \gtrsim 10^9$  K, the star is usually not isothermal: the crust is warmer than the core and thus  $L_\gamma$  is larger than indicated in this figure.

When  $T$  decreases,  $L_\nu^{PBF}$  grows very sharply for each gap when  $T$  reaches the maximum  $T_c$  of the gap reached in the core (PBF neutrino emission turns on) and then decreases with a  $T$  dependence which is between a  $T^8$  and a  $T^7$  power law. This results from the overall  $T^7 F(T/\Delta)$  temperature dependence of the PBF neutrino emissivity combined with the density dependence of  $T_c$  which determines how much of the core, at this given  $T$ , is contributing to  $L_\nu^{PBF}$ . Once  $T$  is much below the minimum value of  $T_c$  reached in the core,  $L_\nu^{PBF}$  becomes exponentially suppressed. In the cases of gaps “b” and “c”, this suppression appears at  $T \ll 10^9$  K, for gap “a” when  $T \ll 2 \times 10^8$  K, whereas for the gaps “T72” this suppression does not appear since  $T_c$  reaches very low values and for any  $T$  there is always a significant volume of the core where  $T \sim T_c$ .

When  $T \lesssim 10^8$  K,  $L_\gamma$  dominates over  $L_\nu$  so that the important range of  $T$  to consider is  $10^8 - 10^9$  K and in this range the figure shows clearly that the relatively small  $n^3P_2$  gaps as “T73” and “a” generate a  $L_\nu^{PBF}$  which is higher, by about one order of magnitude, than the combined  $L_\nu$  that the modified Urca and bremsstrahlung processes would produce when no pairing is present (dashed line in the figure). The modified Urca and bremsstrahlung processes are of course strongly suppressed in the presence of pairing, but these results show that, compared to the no pairing case, pairing can actually *increase* the total neutrino luminosity through the PBF neutrino emission if the gaps have the appropriate size.

Very similar results are obtained when considering the PBF neutrino emission due to the  $p^1S_0$  gaps as shown in Figure 21. The three differences with respect to the  $n^3P_2$  case are, first, that no calculation of the  $p^1S_0$  gap reaches a  $T_c$  as high as our case “c” for the  $n^3P_2$ , second, all  $p^1S_0$

gaps vanish in the inner part of the core which implies that the suppression of  $L_\nu^{PBF}$  at low  $T$  does not show up and, third, the volume of the core in the superconducting state is generally smaller than the volume in the  $n$  superfluid state, resulting in lower values of  $L_\nu^{PBF}$  for  $p$  than for  $n$ .

### 5.5. Comparison of Various Neutrino Luminosities

Having compared, in the previous subsection, the neutrino luminosities from PBF assuming an isothermal interior, we now proceed to analyze them, together with other processes, in realistic cooling calculations which take into account the exact temperature profile within the star. The results are shown in Figure 22. We use a  $1.4 M_\odot$  star built with the EOS of APR and we fix the  $n$  and  $p$   $^1S_0$  gaps considering that the major uncertainty in the neutrino luminosity is due to uncertainty in the size of the  $n$   $^3P_2$  gap (see the results of §5.4). We consider the three cases “a”, “b”, and “c” for the magnitude of the  $n$   $^3P_2$  gap.

The three panels of Figure 22 show clearly that at very early times the cooling is driven by the modified Urca and nucleon bremsstrahlung processes, but that once pairing occurs the neutrino emission from the PBF process takes over because of its efficiency and because the other processes are suppressed.

At ages relevant for the presently available data,  $t \lesssim 10^2$  yrs, we find in all cases that the PBF neutrinos are the main cooling agent, until photon emission takes over at  $t \sim 10^5$  years. There is a competition between the neutrino emission from  $n$   $^3P_2$  and  $p$   $^1S_0$  pairing: the smallest gap drives the cooling between  $10^2$  and  $10^5$  years. With the assumed  $p$   $^1S_0$  gap from AO, we see that in case “a” the  $n$   $^3P_2$  gap drives the cooling (Figure 22 left panel), whereas in case “b” or “c” (Figure 22 central and right panels, respectively) the proton pairing drives the cooling.

This is in agreement with the results of Figure 20 which show that the case “a”  $n$   $^3P_2$  gap is the most efficient and that even smaller gaps, as in T72, do not result in a significant enhancement of the PBF neutrino luminosity or do it too late, i.e., at a time when photon emission dominates the cooling. Comparison of Figure 20 with Figure 21 shows that in the case of a larger  $n$   $^3P_2$

gap, one can expect that the  $p$   $^1S_0$  PBF neutrinos will dominate the cooling, in agreement with our findings of this subsection. Finally we compare cooling trajectories with our three  $n$   $^3P_2$  gaps and a vanishing gap in Figure 23 explicitly confirming that  $n$   $^3P_2$  gaps with  $T_c$  of the order of  $10^9$  K are the most efficient gaps with regard to neutrino cooling through the PBF process.

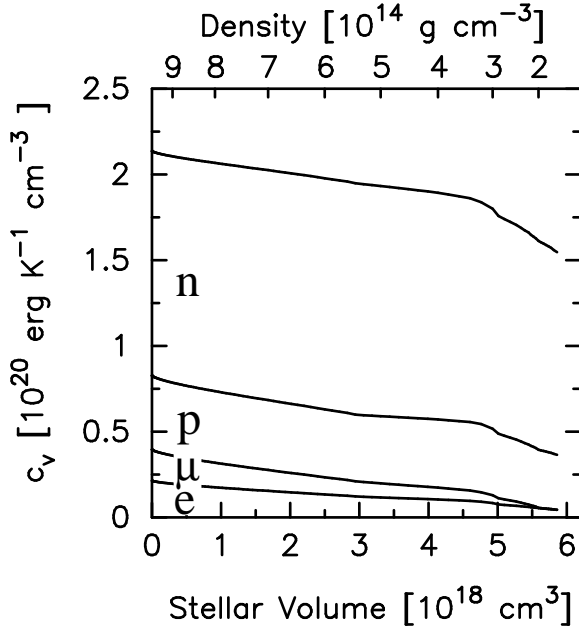


Fig. 11.— Cumulative specific heats of  $e$ ,  $\mu$ ,  $p$ , and  $n$  vs. stellar volume in the core of a  $1.4 M_{\odot}$  star built using the APR EOS, at temperature  $T = 10^9$  K. Nucleons are assumed to be unpaired.

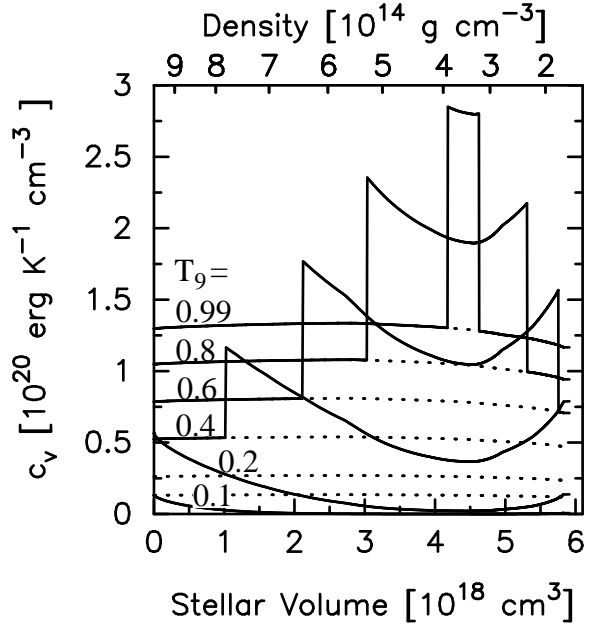


Fig. 12.— Specific heat of neutrons in the core of a  $1.4 M_{\odot}$  star built using the APR EOS, at six different temperatures, from 0.99 down to 0.1 times  $10^9$  K illustrating the effects of pairing. No gap is present for results shown by the dotted lines. The  $n \ ^3P_2$  gap "a" is assumed for continuous curves. This gap has a maximum  $T_c$  of  $1 \times 10^9$  K at  $\rho = 3.61 \times 10^{14}$  gm  $\text{cm}^{-3}$ . the continuous curves show the jump of  $c_v$  by a factor 2.188 (see Figure 13) at the two zones where  $T = T_c$  and its progressive suppression when  $T \ll T_c$  in the layers in between.



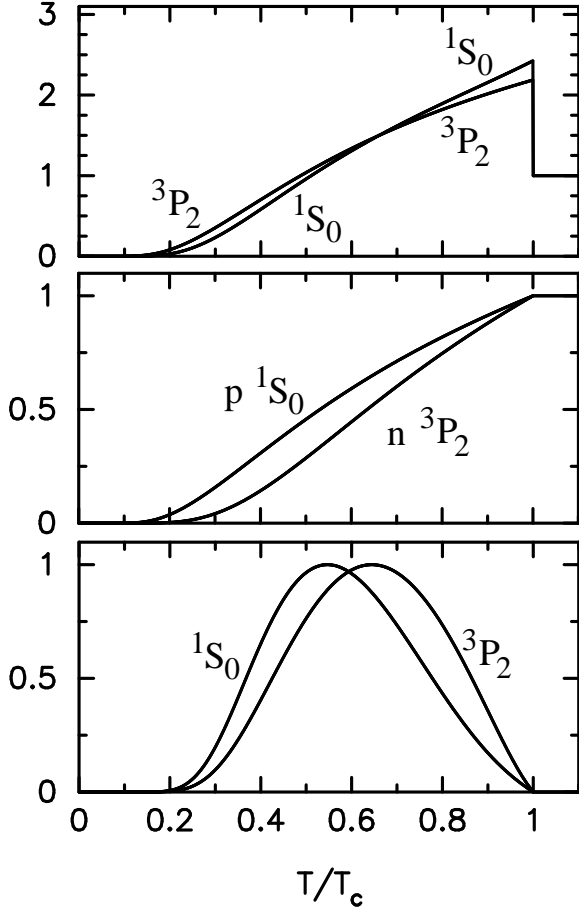


Fig. 13.— Control functions for pairing effects in  $^1S_0$  (for neutrons and/or protons) and  $^3P_2$  (neutrons) channels. The top panel shows the function relevant for the specific heat (§ 3.4), the central panel that for the neutron branch of the modified Urca process with either  $p$   $^1S_0$  or  $n$   $^3P_2$  pairing (§ 3.5) and the bottom panel is for the PBF process (§ 3.5).

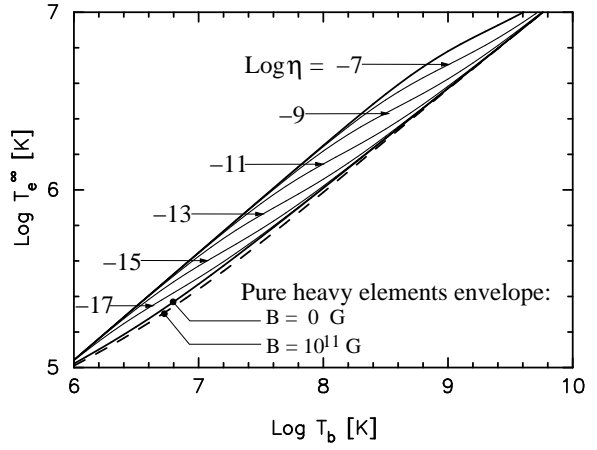


Fig. 14.— Relationship between the effective temperature  $T_e^\infty$  and the interior temperature  $T_b$  at the bottom of the envelope assuming various amounts of light elements parametrized by  $\eta \equiv g_{s14}^2 \Delta M_L / M$  ( $\Delta M_L$  is the mass in light elements in the envelope,  $g_{s14}$  the surface gravity in units of  $10^{14} \text{ cm s}^{-1}$ , and  $M$  is the star's mass), in the absence of a magnetic field (Potekhin, Chabrier & Yakovlev 1997). Also shown are the  $T_e^\infty - T_b$  relationships for an envelope of heavy elements with and without the presence of a dipolar field of strength of  $10^{11} \text{ G}$  following Potekhin & Yakovlev (2001).

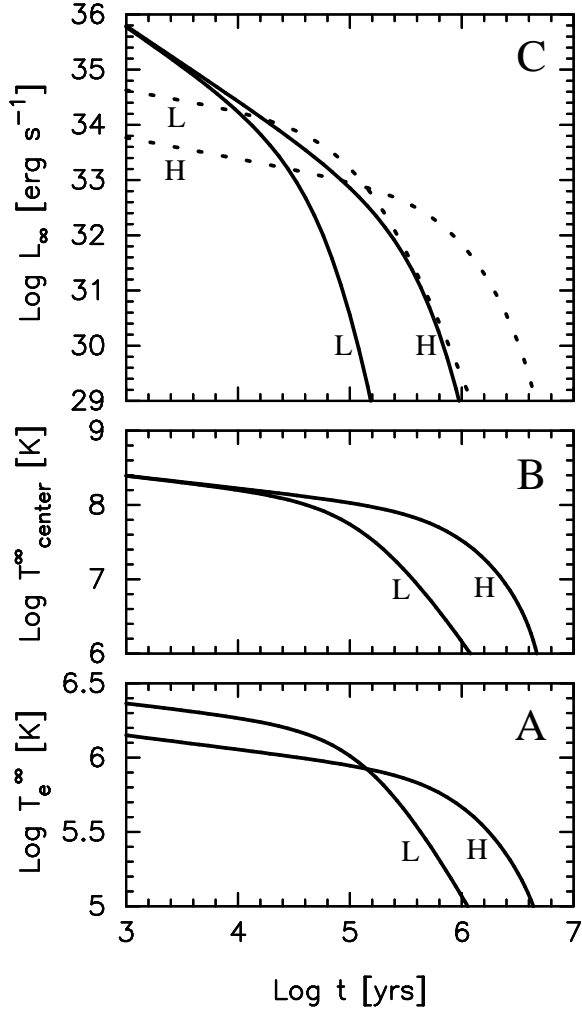


Fig. 15.— Neutrino and photon cooling eras for two models of non magnetized envelopes formed by heavy iron-like elements (labeled “H”) and a maximum amount of light elements (labeled “L”). The effective temperature (panel A), the central temperature (panel B) and neutrino (continuous lines) and photon (dotted lines) luminosities (panel C), all redshifted to infinity, are shown as a function of time. Pairing effects are not included in these calculations.

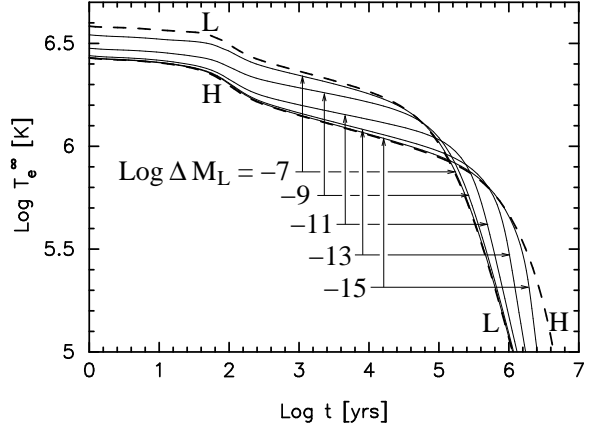


Fig. 16.— Effect on the cooling of various amounts  $\Delta M_L$  (in solar masses) of light elements in the envelope. The two dashed curves, “H” and “L”, are the same as in Figure 15. Pairing effects are not included in these calculations.

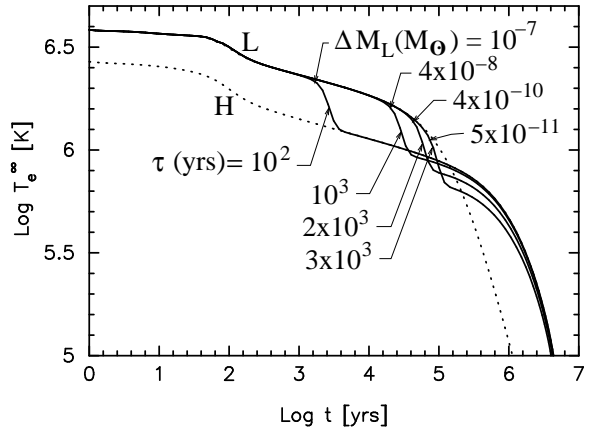


Fig. 17.— Transition of cooling trajectories between a model with a heavy element envelope (dotted curve labeled “H”) and a light element envelope of maximum mass (dotted curve labeled “L”). Continuous curves show evolution of models with “decaying” envelopes (see equation (43)) with various decay times  $\tau$  as indicated. Also indicated are masses of the light element envelopes at the moment the star begins its shift toward the heavy element envelope trajectory.

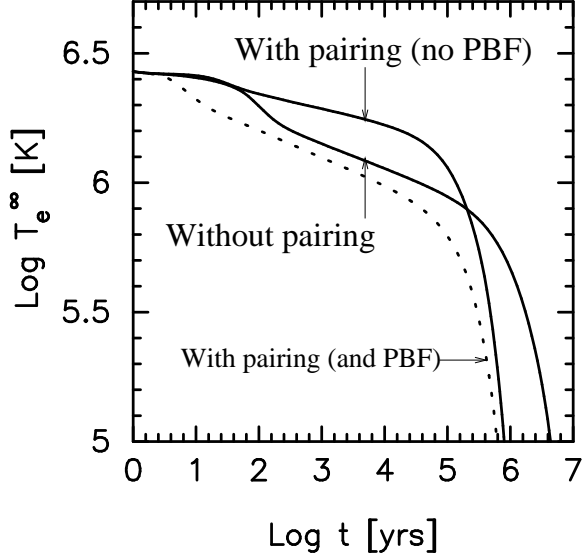


Fig. 18.— Comparison of the cooling of a  $1.4 M_{\odot}$  star, built using the EOS of APR, without and with nucleon pairing. In the model with pairing neutrino emission by the PBF process has been either artificially turned off (continuous line) or allowed (dotted line). Neutron  $^1S_0$  pairing is from AWP,  $^3P_2$  pairing from our case “c” and  $p\ ^1S_0$  pairing from AO, as labeled in Figures 8, 10, and 9, respectively. The envelope is assumed to be composed of heavy elements.

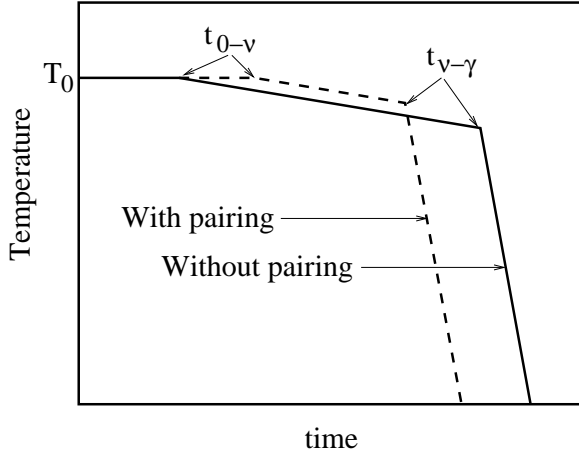


Fig. 19.— Schematic representation of the power-law cooling behaviors and the effect of pairing. The time  $t_{0-\nu}$  denotes when the central temperature falls to a value small enough that  $T \propto t^{-1/6}$  becomes valid. The time  $T_{\nu-\gamma}$  denotes the transition from neutrino to photon cooling eras.

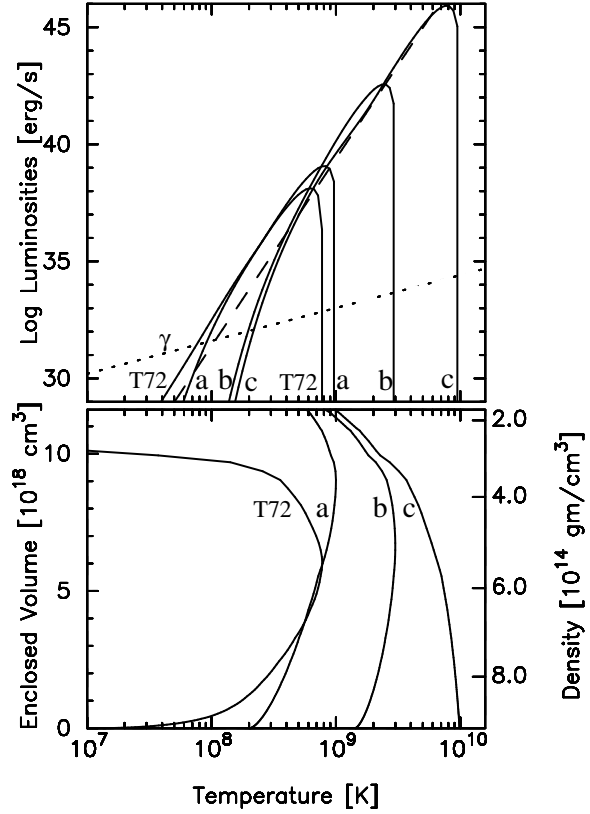


Fig. 20.— Upper panel: neutrino luminosities vs temperature from the PBF process for four different  $n\ ^3P_2$  gaps labeled as in Figure 10. Lower panel:  $T_c$  for the four neutron  $^3P_2$  gaps vs density and enclosed volume.

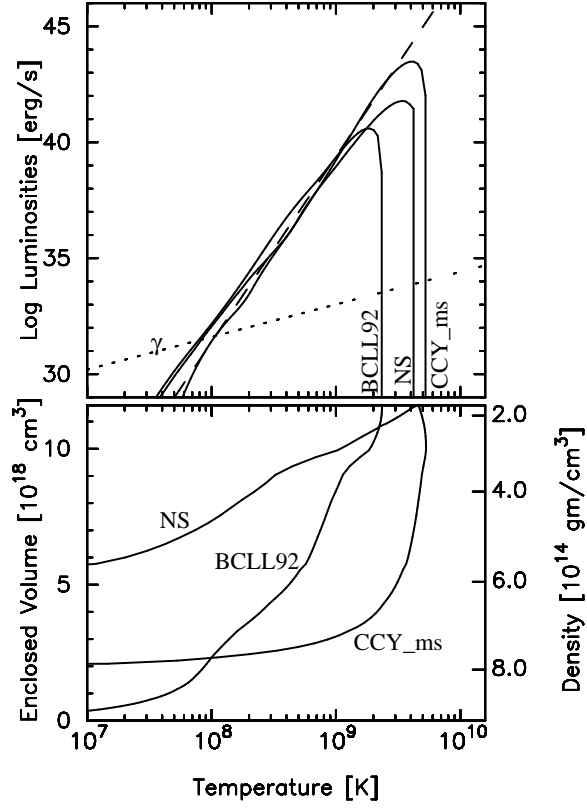


Fig. 21.— Upper panel: neutrino luminosities vs temperature from the PBF process for 3 different  $p^1S_0$  gaps labeled as in Figure 8. Lower panel: critical temperature  $T_c$  for the 3  $p^1S_0$  gaps vs density and enclosed volume.

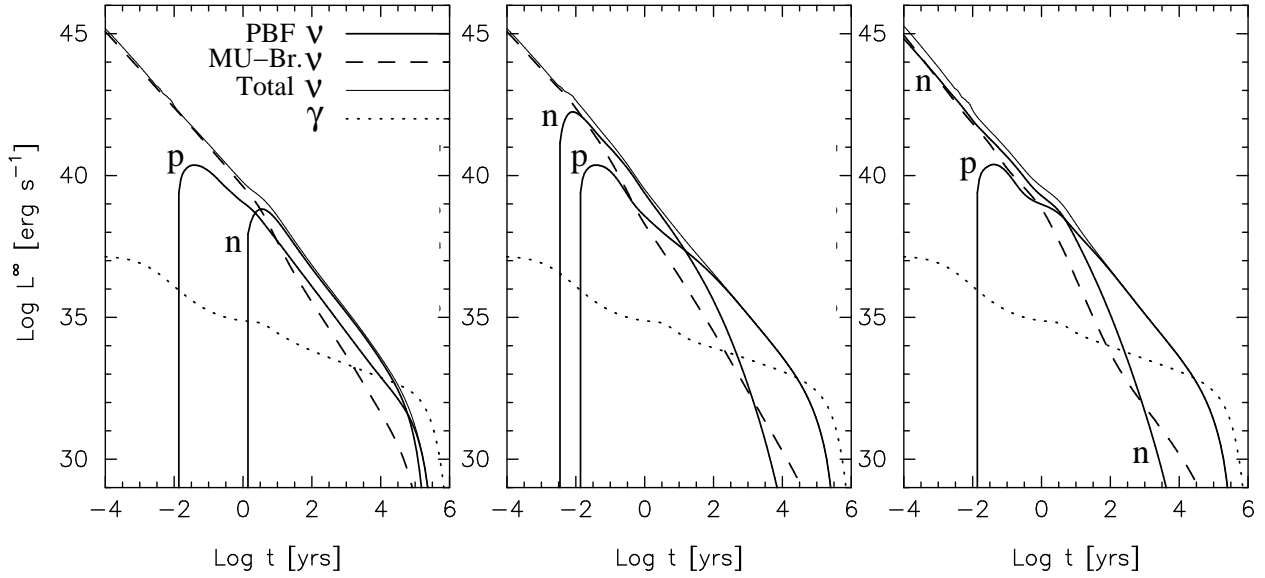


Fig. 22.— Comparison of luminosities from various processes during three realistic cooling histories: photon (“ $\gamma$ ”), all  $\nu$ -processes (“Total  $\nu$ ”), modified Urca and nucleon bremsstrahlung (“MU-Br.  $\nu$ ”), and PBF (“PBF  $\nu$ ”) from  $n$   $^3P_2$  and  $p$   $^1S_0$  pairing marked by “ $n$ ” and “ $p$ ”, respectively. PBF neutrinos from the  $n$   $^1S_0$  gap are not shown explicitly, since their contribution is always dominated by other processes, but they are included in the total  $\nu$  luminosity. In all three cases, the  $p$   $^1S_0$  gap is from AO, the  $n$   $^1S_0$  gap from AWP, whereas the  $n$   $^3P_2$  gap is our model “a” (left panel), “b” (central panel) and “c” (right panel).

### 5.6. More-Modified Urca Cooling

The modified Urca and bremsstrahlung processes all involve four nucleons and are processes in which energy-momentum transfer occurs via strong interactions in the medium. The associated emissivities are sensitive to one's assumptions about in-medium strong interactions and their efficiencies are difficult to assess with certainty. Given this, we consider it important to study the effect of this uncertainty in a simple, but drastic way: we simply multiply the  $q_\nu^{\text{MUrca}}$  and  $q_\nu^{\text{Brem}}$  emissivities by a constant factor  $F$ , taking  $F$  to be 1/10, 10 or 100. A factor 1/10 or 10 could be acceptable, whereas a factor 100 is probably exaggerated.

The results of Figures 20 and 21 showed that in the presence of  $n\ ^3P_2$  and  $p\ ^1S_0$  pairing, most reasonable gaps produce a neutrino emission by the PBF process which is much more intense than the modified Urca and bremsstrahlung in the absence of pairing by at least one order of magnitude in the important temperature range  $T \sim 10^8 - 10^9$  K. Thus, in a realistic calculation a factor  $F = 10$  is not expected to lead to a significant change in the cooling. This is confirmed by our results shown in Figure 24. The models with no pairing clearly show enhanced cooling when  $F = 10$  or 100, and reduce cooling when  $F = 1/10$ , whereas when pairing is included the models with  $F = 10$  and 1/10 are practically indistinguishable from the unenhanced case and only the, probably unrealistic, case  $F = 100$  leads to a faster cooling.

These results are important and fortunate, since they show that the uncertainty in the actual efficiency of the modified Urca rate has no significant effect on the predictions of the minimal scenario when pairing, and the corresponding neutrino emission from the PBF process, is included in a realistic way.

### 5.7. Effects of Neutron Star Mass

In the case that neutrino cooling occurs only through the modified Urca and bremsstrahlung processes, as required by the tenets of the minimal cooling scenario, one can expect that the cooling curves in the neutrino cooling era will show practically no variation with neutron star mass, because there are no energy or density thresholds for these processes. This situation will change drastically for the case in which enhanced cool-

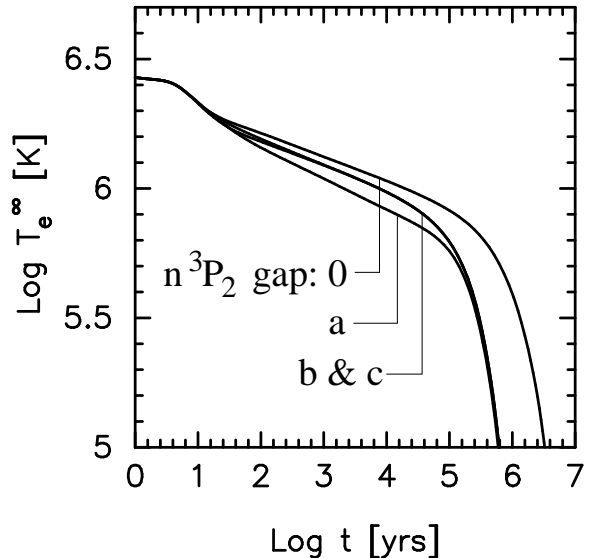


Fig. 23.— Comparison of cooling trajectories with vanishing  $n\ ^3P_2$  gaps, labeled “0”, and our three model gaps “a”, “b”, and “c” (see Figure 10). The  $n\ ^1S_0$  gap is from AWPIII and the  $p\ ^1S_0$  gap from AO (see Figures 8 and 9). Results are for a  $1.4\ M_\odot$  star built using the EOS of APR with a heavy element envelope.

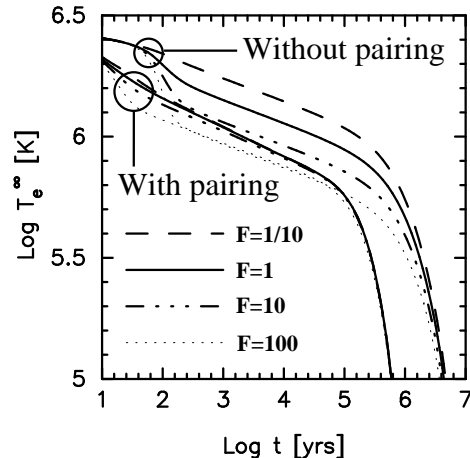


Fig. 24.— Cooling with adjusted modified Urca, for  $F = 1/10, 1, 10$  and  $100$  as indicated, with and without nucleon pairing. Assumed pairing gaps are from our model “a” for  $n\ ^3P_2$  and from AO for  $p\ ^1S_0$  (and  $n\ ^1S_0$  pairing from AWP for which the effect is very small). The envelope is assumed to be composed of heavy elements.

ing through direct Urca processes becomes possible either through nucleons or due to the presence of exotica.

Figure 25 confirms that in the absence of pairing, there is almost no mass effect, both during the neutrino and the photon cooling era. Similarly, when  $n$ , but not  $p$ , pairing is included, the mass dependence is also small, though larger than with no pairing at all. When the  $p$  gap is included, the main variation with mass occurs in the photon cooling era in which more massive stars cool more slowly. This is a direct consequence of the lesser suppression of the proton specific heat with increasing mass, since the  $p$   $^1S_0$  gap vanishes at high density and there is an increasingly larger unpaired region when  $M$  increases ( $C_V(p)$  is larger for larger  $M$ ). The chosen  $n$   $^3P_2$  gap reaches the center of the star in all cases and thus  $C_V(n)$  is strongly reduced for all masses, which explains the small mass dependence when only  $n$  gaps are taken into account. In the case that the  $n$   $^3P_2$  gap would also vanish at high density, we would obtain an additional mass dependence.

### 5.8. Effects of the Equation of State

In exploring the high density EOS, one can expect three sources of effects:

- (1) general relativistic effects due to change in the star's compactness,
- (2) differences in the  $n$  and  $p$  effective masses, and
- (3) differences in the volume of the star in the various paired states.

Figure 26 shows results for the four EOS's selected in § 3.1. When no pairing is included, there is little variation with the EOS, and slight variations exist when pairing is considered. The reasons are essentially the same as those discussed in conjunction with the stellar mass (see the previous subsection) and are due to the density dependence of the  $p$   $^1S_0$  gap and, to a much lesser degree, that of the  $n$   $^3P_2$  gap. The very small differences in the unpaired models simply reflect that the four chosen EOS's are rather similar because of constraints imposed by the minimal cooling scenario: the differences in the stars' compactness and nucleon effective masses are very small.

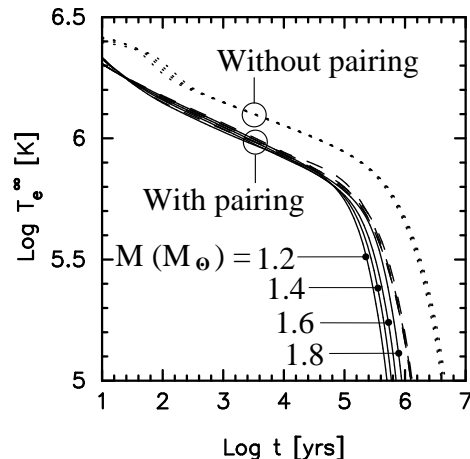


Fig. 25.— Effects of the stellar mass: cooling of stars of various masses built using the EOS of APR, with and without pairing. Models with pairing have  $n$   $^1S_0$  gap from AWP and  $n$   $^3P_2$  gaps from our model “a” and either no  $n$   $^3P_2$  gap (dashed curves) or  $p$   $^1S_0$  gap from AO (continuous curves). Stellar masses are indicated in the cases with the three types of pairing, whereas for similar cases without proton pairing or with no pairing at all the trajectories are too similar to be separately labeled. The envelope is assumed to be composed of heavy elements.

## 6. MINIMALLY COOLING COLDEST NEUTRON STARS

One of the main goals in this work is to determine how cold an observed neutron star should become to be incompatible with the predictions of the minimal scenario. Armed with the results of the previous section, we can now identify the fastest cooling models within this scenario.

### 6.1. Neutrino cooling era

During the neutrino cooling era, Figure 23 shows that the lowest  $T_e$ 's are obtained due to the PBF process when the  $n^3P_2$  gaps are of the size of model “a”, i.e., with  $T_c$ 's of order at most  $10^9$  K in most of the stellar core. The  $p^1S_0$  gaps cannot compete with the most efficient  $n^3P_2$  gaps, because proton gaps are restricted to a smaller volume; compare Figures 20, 21, and 22. These fastest neutrino cooling models have a very weak dependence on the mass of the star (Figure 25). These models also require that the envelope be made of heavy elements or, if it contains light elements, their amounts should be much smaller than  $10^{-11} M_\odot$  (see Figure 16).

### 6.2. Photon cooling era

The physical processes that control cooling in the photon cooling era are quite different from those in the neutrino cooling era. Neutrino emission from any of the possible processes make only a small contribution in the photon cooling era.

The two crucial ingredients are the envelope, which determines the photon luminosity and the specific heat, which controls pairing (see § 5.1). A light element envelope, producing a higher  $T_e$  and hence a higher  $L$  for a given core temperature, leads to fast cooling; an amount above  $10^{-9} M_\odot$  of these elements is necessary (see Figure 16). Concerning the total specific heat, the strongest reduction can be achieved by pushing baryon pairing to the extreme, and this means considering low mass neutron stars so that the  $p^1S_0$  gap is more likely to reach the center of the star. Pursuing the trend indicated in Figure 25, we consider effects of the various  $p^1S_0$  gaps of Figure 9 for a low mass,  $1.1 M_\odot$ , neutron star. Results are shown in Figure 27. The proton  $k_F$  at the center of this star has a value of  $1.1 \text{ fm}^{-1}$  (see Figures 5 and 6); the inset of Figure 27 shows a direct mapping of

the density at which the  $p^1S_0$  gap vanishes with  $T_e$  at these times. The fastest cooling model corresponds to the  $p^1S_0$  gap “CCDK,” which has a  $T_c$  of  $1.44 \times 10^9$  K at the center of the star and hence produces a complete suppression of the proton specific heat in the photon cooling era. A  $p^1S_0$  gap with a higher  $T_c$  at the center of the star, or a gap that vanishes at higher densities (not reached in this star), would lead to the same cooling curve. Similar considerations apply to the  $n^3P_2$  gap. To illustrate this, we used our model gap “a” in Figure 27. Any other gap with a  $T_c$  higher than a few times  $10^8$  K would result in the same total suppression of the neutron specific heat and, therefore, to exactly the same cooling curve.

These results will be important when comparing our predictions with data in the next section, particularly for young stars with ages of the order of a few times  $10^4$  years, such as the Vela pulsar and PSR 1706-44.

## 7. COMPARISON OF THE MINIMAL COOLING SCENARIO WITH DATA

In § 5, we analyzed in some detail the effect of each physical ingredient that shapes the cooling history of a neutron star within the minimal scenario. In § 6, we identified the fastest cooling neutron star models in this scenario. The combined effects of these ingredients in realistic models, together with comparisons to the presently available temperature and luminosity measurements, are presented below.

Our task is greatly simplified by the fact that the EOS is considerably constrained by the tenets of the minimal scenario (see results of § 5.8). Moreover, as shown in § 5.7, the precise mass of the neutron star also has little effect, with the possible exception of low mass stars at ages around a few times  $10^4$  years. (This, of course, is changed drastically once we go beyond the minimal scenario and allow for enhanced neutrino emission processes to occur at high density.) We can therefore restrict our attention mostly to the thermal evolution of a “canonical”  $1.4 M_\odot$  neutron star built with the EOS of APR. In contrast, the chemical composition of the envelope and the extent of pairing of both neutrons and protons will play significant roles.

As shown in § 5.1, the presence of light elements



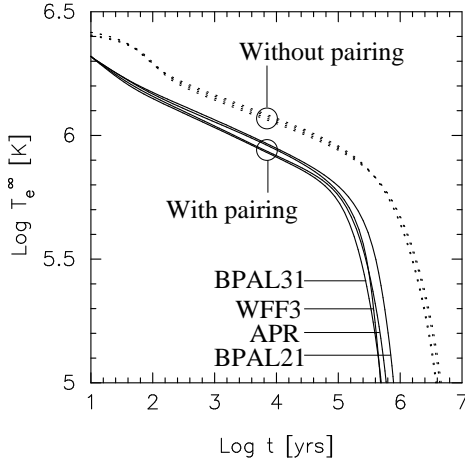


Fig. 26.— Effects of the EOS: cooling of  $1.4 M_{\odot}$  stars built using the four chosen EOS's. EOS's are labeled in the cases with pairing, whereas for similar cases without pairing the trajectories are too similar to be separately labeled. Pairing gaps:  $n \ ^1S_0$  from AWP,  $n \ ^3P_2$  from our model “a” and  $p \ ^1S_0$  from AO. The envelope is assumed to be composed of heavy elements.

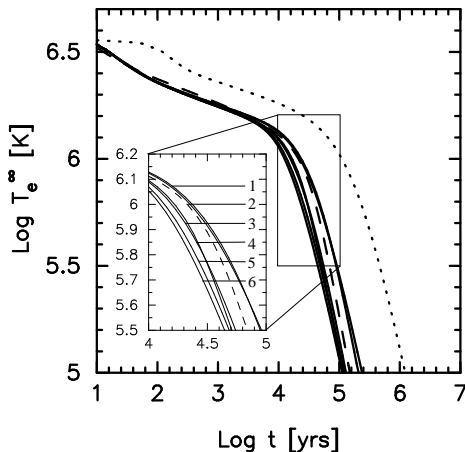


Fig. 27.— Cooling of a  $1.1 M_{\odot}$  star (continuous lines) and with various  $p \ ^1S_0$  gaps (as labeled in the inset): 1 - NS, 2 - T, 3 - AO, 4 - BCLL, 5 - CCY\_ms, and 6 - CCDK (see Figure 9 for notation). The  $n \ ^1S_0$  gap is from AWP, and the  $n \ ^3P_2$  gap from our model “a”. The dotted line is the same  $1.1 M_{\odot}$  star, but without any pairing and the dashed line is for a  $1.4 M_{\odot}$  star, with the same pairing gaps as in Figure 25. Envelopes are all assumed to be composed of light elements.

in the envelopes of young neutron stars leads to effective temperatures that are larger than those without any light elements during the neutrino cooling era, whereas it implies a faster cooling during the later photon cooling era. Thus, for an assumed high density structure of the star, there exists a whole family of models limited by the two extreme cases of envelopes: those with only heavy elements, and those with a maximum amount of light elements. Stars with envelopes containing only a small amount of light elements will evolve on intermediate tracks shifting from a track close to the former one toward the latter one as illustrated in Figure 16. Conversely, stars can evolve in the opposite direction if the envelope composition changes with time from light elements toward heavy elements; such an evolution is very abrupt as shown in Figure 17.

On the other hand, the occurrence of pairing also accelerates cooling during the photon cooling era through the reduction of the specific heat (see § 5.3), whereas pairing effects during the neutrino cooling era are more delicate. Neutrino emission from the modified Urca and bremsstrahlung processes is suppressed, but the breaking and formation of Cooper pairs can easily, with appropriate gaps, become vastly more efficient than the former processes. As a result, depending on its size and density dependence, pairing can lead to faster or slower cooling during the neutrino cooling era; its effect has to be considered carefully.

Our main results are presented in Figure 28 and compared with data. For the reasons discussed in § 2.3, we present them in two forms: effective temperature  $T_e^{\infty}$  versus time and luminosity  $L^{\infty}$  versus time. We divide our results into three subclasses depending on the size of the  $n \ ^3P_2$  gap, given that this gap is the most uncertain one: a vanishingly small gap and our gap models “a” and “b”. Figures 22 showed that case “c” results in neutrino emissions very similar to that of model “b” and Figure 23 confirmed that the resulting cooling trajectories are practically identical for these two large  $n \ ^3P_2$  gaps and we therefore do not need to include results for the gap “c” here. For each assumed neutron  $^3P_2$  gap, it is still necessary to consider uncertainties in the  $n$  and  $p \ ^1S_0$  gaps. Varying these gaps is less dramatic than varying the  $n \ ^3P_2$  gap and we consider 15 different combinations (see the caption of Figure 28)

which we plot together. We obtain, for each assumed  $n^3P_2$  gap, two sets of very closely packed curves, one for each envelope composition. The size and extent of the  $n^1S_0$  gap has very little effect, since it is mostly restricted to the crust and encompasses only a small part of the star’s volume. This leads to small differences in the early cooling when the star has not yet reached isothermality, at ages  $\sim 3 - 100$  years, and the surface temperature is still controlled by the evolution of the crust. Among the  $p^1S_0$  gaps, the ones which can reach higher densities will lead to slightly faster cooling both during the neutrino cooling era, because of the enhanced neutrino emission from the PBF process, and during the photon cooling era, due to the resulting smaller specific heat.

Figure 23 demonstrated that models with the  $n^3P_2$  gap “a” yield the coldest stars and Figure 28 shows that the spread in results due to the variation of the other two  $^1S_0$  gaps is much smaller than in the other two scenarios. This is because the  $n^3P_2$  gap “a” maximizes neutrino emission by the PBF process (see Figure 20) and because the neutrino luminosity due to the proton PBF process is lower (compare Figure 21 with Figure 20). We have studied many other models with a  $n^3P_2$  gap similar to our case “a”, but with slightly different maximum values of  $T_c$  and different density dependences, and discerned negligible differences. We are thus confident that the results presented here reflect the smallest temperatures possible within the constraints of the minimal scenario. We can obtain a slightly faster cooling in the photon cooling era for low mass neutron stars (near 1 to 1.2  $M_\odot$ ) as discussed in § 6, and this case will be presented separately at the end of this section.

We now compare observational data for specific neutron stars with the suite of models encompassing the minimal cooling scenario.

### 7.1. RX J0822-4247 and 1E 1207-52

These two are young and are the hottest known stars. Their inferred temperatures are higher than the predictions of all our models with heavy element envelopes, but are compatible with all models with light element envelopes. This may be considered as possible evidence for the presence of a significant amount of light elements in the upper layers of these stars. However, when considering luminosities, for select values of the

$n^3P_2$  gap, 1E 1207-52 is compatible with having an heavy elements envelope. RX J0822-4247, however, remains more luminous than any of the heavy-element envelope models but is compatible with light-element envelope models.

### 7.2. PSR 0656+14, PSR 1055-52, Geminga, RX J1856.5-3754, and RX J0720.4-3125

These are the five oldest observed stars. Fits of their spectrum to light-element atmospheres result in radii too large to be compatible with the neutron star hypothesis. Blackbody spectral fits result in too-small radii, but it is possible for heavy-element atmospheres or two-temperature black bodies to be constructed that produce compatible radii. For consistency, we have restricted the data appearing in these plots to be a result of either light-element atmosphere fits or single-temperature blackbody fits. Inferred temperatures are more sensitive to the assumed atmospheric composition than are luminosities, and for these five objects, the  $L$  versus age plots are probably more reliable and representative of the observational uncertainties. Consequently, blackbody fits result in relative positions for temperatures that are quite different than those of the luminosities.

Except for RX J1856.5-3754, the large uncertainties on the age and the luminosity of these objects preclude definite conclusions. If we consider the upper limits to their age and/or luminosities, we find them too bright and must invoke the presence of some strong heating process. On the other hand, considering the lower limits to ages and/or luminosities they appear compatible with the minimal scenario independently of assumptions about pairing.

### 7.3. Vela, and PSR 1706-44

Very intriguing objects are the pulsars PSR 0833-45 (“Vela”) and PSR 1706-44. Vela has been repeatedly proposed as a candidate for enhanced cooling or exotic matter, but our results are inconclusive with respect to these claims. For this star, the effective area is compatible with emission from almost the entire surface of a neutron star and both types of plots,  $T$  or  $L$  vs age, are equivalent. With an  $n^3P_2$  gap chosen to maximize

neutrino emission from the PBF process, as in our case “a”, the discrepancy of Vela with the theoretical prediction is not significant whereas for a vanishing  $n\ ^3P_2$  gap it is very large. However, for any non-vanishing  $n\ ^3P_2$  gap and a low assumed stellar mass (see Figure 29), several of the light element envelope models reach the temperature of Vela at an age of 20,000 yrs, i.e., well within its age uncertainty and even less than some estimates of the supernova remnant age,  $1.8 \pm 0.9 \times 10^4$  yrs (Aschenbach, Egger & Trümper 1995). These models correspond to  $p\ ^1S_0$  gaps which extend to relatively high densities and hence result in strong suppression of the proton specific heat in most of, if not all, the core (see § 6). An interesting feature of these models is the very fast decrease of temperature

$$\frac{\Delta T_e}{T_e} \sim -0.85 \frac{\Delta t}{t}, \quad (44)$$

which for an age of 20,000 yrs gives a decrease of the observable x-ray flux of 0.17% every decade. In this case one could interpret these results as indicating that the Vela pulsar is a low mass neutron star with a thick light element envelope and in which neutrons and protons are paired in the entire core. On the other hand, they could favor a neutron star whose core neutrons have a  $T_c$  of the order of  $10^9$  K, without any constraint about the proton pairing and the stellar mass, but this star must have a heavy element envelope with at most  $10^{-13} M_\odot$  of light elements at the surface (see Figure 16).

PSR 1706-44 is in a similar situation, but with larger uncertainties both in  $T$  and in  $L_\infty$ , due to the large distance and age uncertainties. Confirmation of its association with the supernova remnant G 343.1-2.3 (McAdam, Osborne & Parkinson 1993) would help constrain both its distance and age.

#### 7.4. Barely detected and undetected objects

Sources that have negligible or no observed thermal emissions, listed in Table 3 and plotted in Figure 2, are compared with our results in Figure 30. The upper luminosity limits for the two objects CXO J232327.8+584842 (in Cas A) and PSR J0154+61 are well within the prediction of the minimal scenario whereas the limit of PSR

J1124-5916 is on the lower side, but still compatible.

Most interesting are the two stars PSR J0205+6449 (in 3C58) and RX J0007.0+7302 (in CTA 1) whose upper limits are clearly below our predictions. The remaining four objects, with no point-like emissions of any kind observed to date, would provide definitive evidence for enhanced cooling if it could be shown that neutron stars in fact exist in any of them.

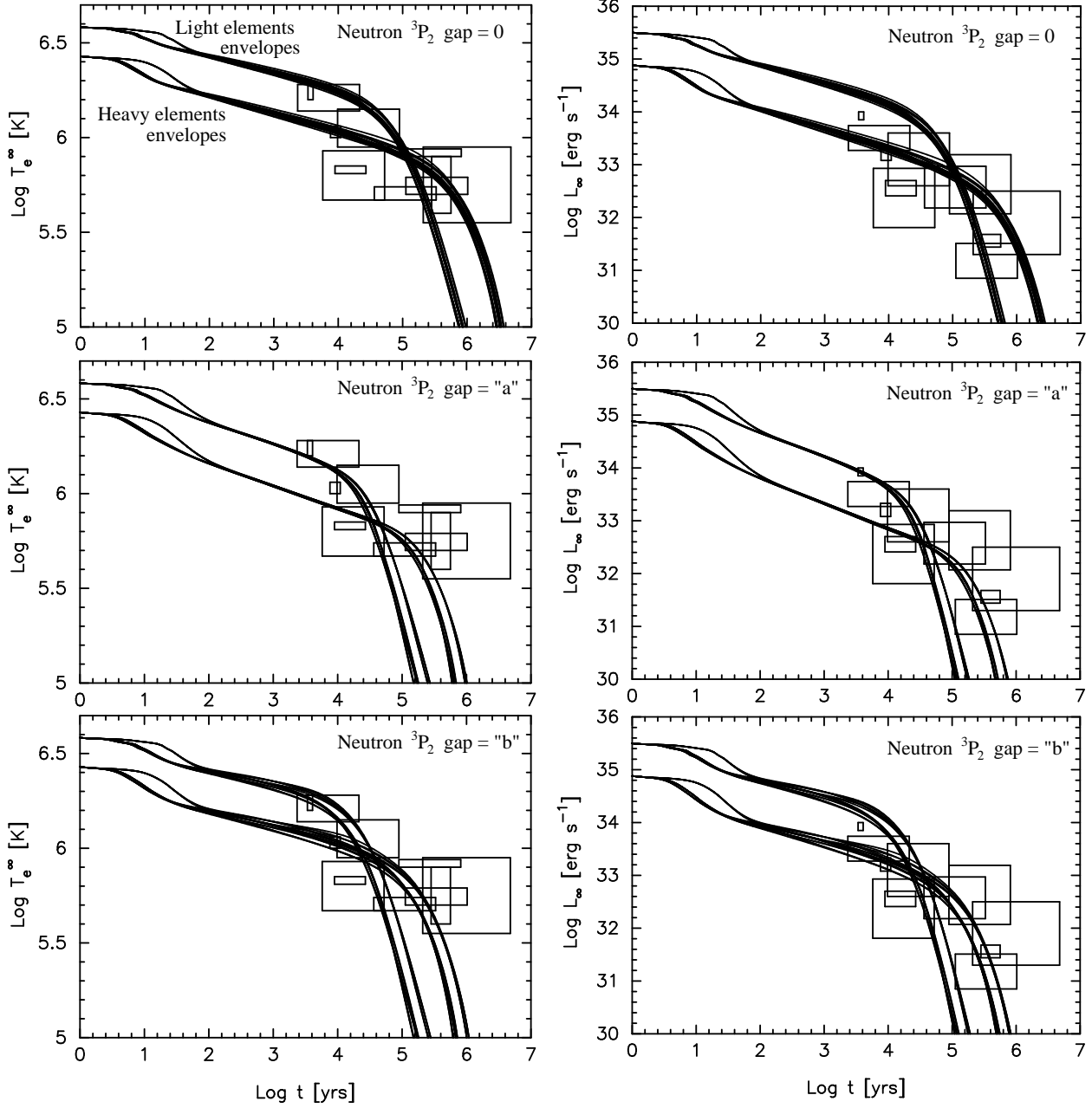


Fig. 28.— Comparison of predictions of the minimal cooling scenario with data, all models being  $1.4 M_{\odot}$  stars built using the EOS of APR. Left panels: effective temperature  $T_e^{\infty}$  vs. age. Right panels: luminosity  $L_{\infty}$  vs. age. The upper, middle, and lower panels correspond to three different assumptions about the size of the  $n {}^3P_2$  gap as indicated in the panels. In each panel, the two sets of curves correspond to the two extreme models of envelope chemical composition: light elements or heavy elements, as labeled in the upper left panel. For each set of curves, the 15 different curves correspond to three different choices of the  $n {}^1S_0$  gap (“AWPII”, “AWPIII”, and “SCLBL” as labeled in Figure 8) and five different  $p {}^1S_0$  gaps (“CCYms”, “T”, “NS”, “AO”, and “BCLL” as labeled in Figure 9).

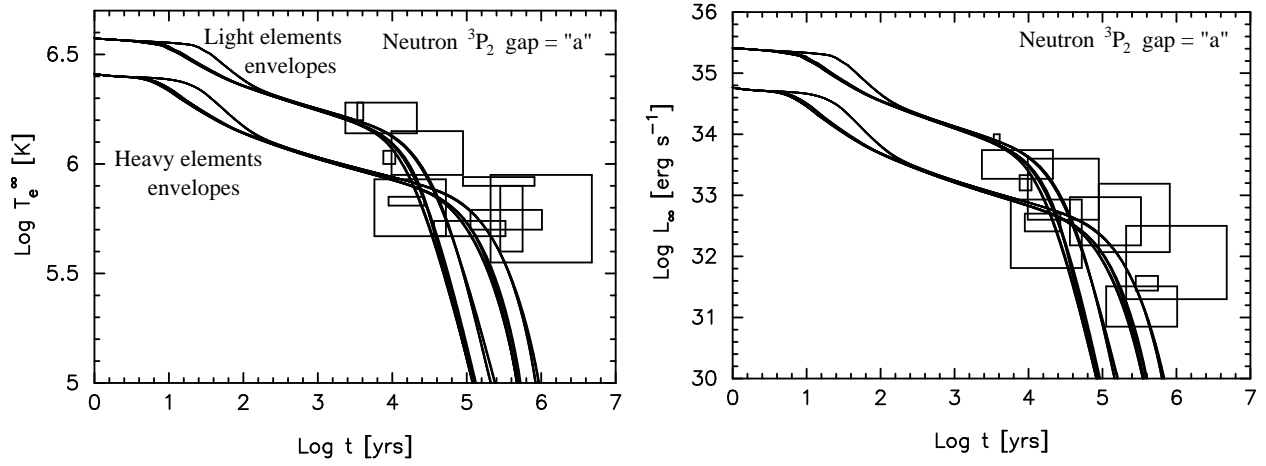


Fig. 29.— Same as the central panels of Figure 28, but for a  $1.1 M_\odot$  star built using the EOS of APR.

## 8. COMPARISON WITH OTHER WORKS

The literature on neutron star cooling is extensive and dates back to the early 60's. Detailed studies of the “standard” cooling of isolated neutron stars have been presented, e.g., by Nomoto & Tsuruta (1987), van Riper (1988), and Schaab et al. (1996), but none of these works had included the neutrino emission from the PBF process. Models incorporating the PBF process were first presented by Schaab et al. (1997) and subsequently by Page (1998). These two works, however, did not explore effects of various EOS's and/or various sets of pairing gaps within the framework of the “standard” scenario. Our present results are in agreement with the results of Nomoto & Tsuruta (1987), van Riper (1988) and Page (1998) when similar input physics are used and allow a close comparison.

We find, however, large differences with the results of Schaab et al. (1996) and Schaab et al. (1997) during the photon cooling era in which the models of these authors cool much more slowly than our models. This discrepancy is probably attributable to differences in the specific heat. For example, during the photon cooling era, the Schaab et al. models in which pairing is considered cool in almost the same way as models in which the effects of pairing are neglected. The models without pairing have luminosities about one order of magnitude higher than our corresponding models at ages in the range  $10^6 - 10^7$  years.

Extensive calculations of the effect of the PBF process have been presented by Levenfish, Shibano & Yakovlev (1999) in a simplified model in which both the  $p\ ^1S_0$  and  $n\ ^3P_2$  gaps were assumed to be constant in the entire core of the star. This simplification of uniform  $T_c$  (which implies that protons are paired in the entire core of their stars, whereas in our models the protons in the central part of the star are unpaired for  $1.4\ M_\odot$  stars) has the effect of overestimating the neutrino emission by the PBF process. Their results are consistent with our findings in that they obtain somewhat cooler stars. For example, they can reach  $\log T_e^\infty = 5.8$  at age  $t = 10^4$  years, whereas our coolest model with  $n\ ^3P_2$  gap of our model “a” has  $\log T_e^\infty = 5.9$  at the same age.

Subsequent works of Yakovlev et al. (2002) and Yakovlev & Haensel (2003), which explored more

realistic, density-dependent gaps, obtained results which are in good agreement with ours. For models in which no enhanced neutrino emission is at work, these two works obtain a minimal  $\log T_e^\infty$  of 5.9, as we do, at an age of  $t = 10^4$  years.

Several recent works, Kaminker, Haensel & Yakovlev (2001), Yakovlev, Kaminker & Gnedin (2001), Kaminker, Yakovlev, & Gnedin (2002), and Tsuruta et al. (2002), studied the cooling of neutron stars within the “standard” scenario (including the PBF processes), but with enhanced neutrino emission at high density. In addition, they did not explore the range of parameters that are considered here. Consequently, these studies cannot be compared to the minimal scenario presented here.

In a recent review, Yakovlev & Pethick (2004) have examined standard and enhanced cooling in an attempt to fit all the data within one model. In this work, the data on individual objects are fit by treating the mass of the star as a free parameter. Models in which the  $n\ ^3P_2$  gap is taken to be vanishingly small (Schwenk & Friman 2004) are favored, together with a  $p\ ^1S_0$  gap that persists up to very high densities and with a  $T_c$  of the order of  $7 \times 10^9$  K. This latter feature is incompatible with all calculations of this gap we report in Figure 9, but is not absolutely excluded. Our models for  $1.1\ M_\odot$  with nucleon pairing in the entire core (see Figure 29) are similar to those of Yakovlev & Pethick with non-vanishing  $n\ ^3P_2$  gaps, whereas our models of heavier stars with extensive neutron pairing but a large volume of unpaired protons are similar to their models with vanishing  $n\ ^3P_2$  gaps and extensive proton pairing (see Figures 28).

## 9. DISCUSSION AND CONCLUSIONS

We have presented a detailed study of the thermal evolution of an isolated neutron star using what we term as the minimal cooling scenario. This scenario is an extension of the well-known “standard cooling” scenario to include the effects of nucleon pairing and complements neutrino emission by the modified Urca and nucleon bremsstrahlung processes with the pair breaking and formation (PBF) process. We have confirmed the results of previous works by others that for many models of nucleon pairing, the PBF process actually dominates the cooling of the star (see

§ 5.4) and hence is an essential ingredient of the minimal cooling scenario.

Among the four parameters we proposed for an overall classification of neutron star cooling models, we found that the EOS at supranuclear densities is well constrained by the requirements of the minimal cooling scenario. Moreover, we showed that the stellar mass has little effect on the results. We emphasize that for scenarios beyond the minimal one, i.e., when new particles and neutrino emission processes appear, these two parameters definitely gain importance. The other two parameters we considered, pairing properties of the nucleons and chemical composition of the envelope, introduce the largest uncertainties in our theoretical predictions.

We singled out three subclasses of scenarios due to uncertainties in the size and extent of the  $n$   $^3P_2$  gap. For this gap, we considered three different cases: a vanishingly small gap, a somewhat small gap (our model “a”) and a relatively large gap (model “b”). Within each of these cases, variations of the  $n$  and  $p$   $^1S_0$  gaps covering the published ranges of these gaps were also considered.

With respect to the chemical composition of the envelope, we singled out two extreme cases: an envelope consisting of heavy iron-like elements and an envelope containing essentially only light elements. For each choice of the  $n$   $^3P_2$  gap, we obtained two families of closely packed cooling curves representing each of the two extreme envelope cases, with some spreads due to variations of the  $n$  and  $p$   $^1S_0$  gaps. Intermediate envelope chemical compositions, or its possible temporal evolution, result in cooling trajectories intermediate between the extremities (see Figures 16 and 17).

Comparing our results with observationally inferred temperatures  $T_\infty$  and luminosities  $L_\infty$  of eleven isolated neutron stars (Figures 28 and 29), we found that the observations were in overall good agreement with the minimal cooling scenario taking into account the uncertainties of envelope and pairing properties as well as those of the ages and inferred  $T_\infty$  and  $L_\infty$  for these stars. It is probably not possible to understand these data within a single model with a unique envelope chemical composition. Considering that the compositions of the upper layers are strongly dependent on poorly understood processes which occurred dur-

ing and soon after the birth of the star, and possibly later due to the dynamics, it appears likely that different stars have envelopes with different chemical compositions.

The Vela pulsar 0833-45, and possibly, but with much larger uncertainties, PSR 1706-44, are marginal candidates for enhanced cooling as their inferred temperatures and luminosities are lower than most of our models. Nevertheless, we found that low mass neutron stars,  $\sim 1.1 - 1.2 M_\odot$ , with a light element envelope and extensive nucleon pairing covering essentially the entire core, could reach the inferred values,  $T_\infty \simeq 10^{5.8}$  K at an age of  $\sim 20,000$  years (Figure 29) which is within the range of estimated age of the associated supernova remnant.

An essential component of the minimal cooling scenario is neutrino emission by the PBF process, which leads, in the presence of appropriate nucleon gaps, to more rapid cooling than possible in the standard cooling scenario. The low observed temperatures of the two pulsars, Vela and 1706-44, can be accommodated by the PBF process with a  $n$   $^3P_2$  gap of sufficient size. However, if this gap were vanishingly small (Schwenk & Friman 2004), then the temperature and thermal luminosity measurements of these two objects would be evidence for the presence of processes beyond the minimal cooling paradigm.

The five older stars, PSR 0656+14, PSR 1055-52, PSR 0633+1748 (Geminga), and RX J0720.4-3125, unfortunately have such large uncertainties on both their ages and thermal luminosities that their interpretation is delicate. They do not require the occurrence of enhanced neutrino emission and can be accommodated within the minimal cooling scenario when the lowest values for  $T$  and  $L_\infty$  are chosen. But, should the upper limits for  $T$  and  $L_\infty$  prevail, they would be good candidates for the occurrence of some “heating mechanism”, i.e., dissipative processes, which inject heat into the star (see, e.g., Umeda et al. (1993) & Schaab et al. (1999)). In the case of RX J1856.5-3754, which has a much more tightly constrained age and luminosity, the agreement with the minimal scenario is excellent.

The two objects standing apart from the other observed neutron stars are J0205+6449 (in the supernova remnant 3C58) and RX J0007.0+7302 (in CTA 1). Upper limits on their luminosities are

well below the predicted values for any of our models. These two objects are the best candidates, to date, for the necessity to go beyond the minimal scenario.

Finally, the four upper luminosity limits on the undetected objects in shell supernova remnants (G084.2-0.8, G093.3+6.9, G127.1+0.5, and G315.4-2.3) recently found by Kaplan et al. (2004) are so low that they will constitute the strongest evidence for enhanced neutrino emission well beyond the minimal scenario if it can be demonstrated that they actually correspond to neutron stars and not quiescent black-holes.

The authors wish to acknowledge many discussions over the years with D. G. Yakovlev and O. Y. Gnedin, including extensive exchanges of numerical results to compare our two, independently developed, cooling codes. This work was supported by a binational (NSF-Conacyt) US-Mexico grant. DP acknowledges extra support from grants UNAM-DGAPA (#IN112502) and Conacyt (#36632-E). JL, MP, and AS acknowledge research support from the U.S. DOE grants DE-AC02-87ER40317 and DE-FG02-88ER-40388, and the NSF grant INT-9802680.

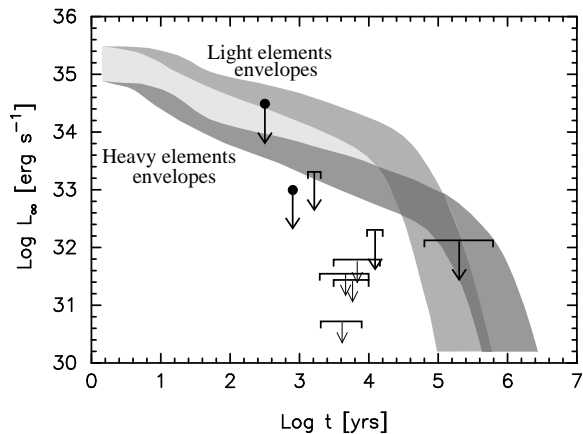


Fig. 30.— Global comparison of the upper luminosity limits for sources lacking apparent thermal emissions with cooling trajectories, satisfying the minimal cooling scenario. The area with the darkest gray shading contains models with heavy-element dominated envelopes, whereas that with the intermediate shading contains models with light-element envelopes. The region with the lightest shading contains models with intermediate compositions.



## A. Observational Data

### A.1. Supernova Remnants G084.2-0.8, G093.3+6.9, G127.1+0.5, & G315.4-2.3

These four SNR's are considered to be the product of core-collapse supernovae and are hence expected to contain either a neutron star or a black-hole. Nevertheless, the searches of Kaplan et al. (2004) found no evidence of any sort for the presence of compact objects. In case a neutron star is present, these observations provide us with upper limits on the thermal luminosity of the star which we take from the Figure 37 of Kaplan et al. (2004) and report in our Table 3.

### A.2. CXO J232327.8+584842 in Cas A

Discovered in the first light of the *Chandra* observatory, this object is still enigmatic but evidence points toward an isolated neutron star (Mereghetti et al. 2002). We take the upper limit on  $L_\infty$  from Pavlov et al. (2000), which results from a composite model of a hot polar cap and a warm (but barely detected) surface. The age is from the association with the supernova SN 1680.

### A.3. PSR RX J0205+6449 in 3C58

A first upper limit on  $T_\infty$  had been obtained by Slane, Helfand & Murray (2002) from the non detection of a thermal component in the pulsar spectrum. Analysis of a deeper *Chandra* observation (Slane et al 2004b) requires the presence of a thermal component and leads to a lower upper limit on  $L_\infty$  reported in Table 3. This value is a conservative estimate since even lower values are possible when an atmosphere model is used in the spectral fits. The association with the historical remnant of SN 1181 gives an age of 822 years. The pulsar spindown age is about 5400 years (Murray et al. 2002). The distance estimate is from 21 cm (HI) absorption (Roberts et al. 1993).

### A.4. PSR J1124-5916 in G292.0+1.8

This x-ray and radio pulsar is seen as a point source in a composite SNR. The *Chandra* spectrum of the pulsar (Hughes et al. 2003) is adequately fit by a power law, with no evidence for thermal emission, and provides an upper limit on the thermal luminosity. Distance and kinematic age estimates are taken from Camilo et al. (2002).

### A.5. PSR RX J0822-4247 in Puppis A

The ages are taken from spin-down (8000 years) and from motions of filaments in the Puppis A supernova remnant. The distance is estimated from 21 cm (H) absorption. Both quantities are discussed in Zavlin, Trümper & Pavlov (1999) and references therein. Blackbody and H atmosphere spectral fitting, from ROSAT and ASCA data, are also from Zavlin, Trümper & Pavlov (1999).

### A.6. PSR 1E 1207-5209 in G296.9+10.0

Estimates of the kinematic age are from Roger et al. (1988) and the distance are from Giacani et al. (1988). The spindown age is from Pavlov et al. (2002). Blackbody spectral fitting is from Mereghetti, Bignami & Caraveo (1996) from ROSAT and Zavlin, Pavlov & Trümper (1998) from ROSAT + ASCA.

This is one of the very few isolated neutron stars which shows spectral lines in its spectrum (Sanwal et al. 2002), but the phase variation of these lines (Mereghetti et al. 2002) may indicate they are of magnetospheric origin. Moreover, its peculiar spin-down behavior may be a sign of accretion, making the interpretation of this star as an isolated cooling neutron star questionable (Zavlin, Pavlov & Sanwal 2004).

### A.7. RX J0002+6246

Spectral fitting for both H atmosphere and blackbody surfaces are from *Chandra* observations (Pavlov 2002), and are consistent with ROSAT observations reported by Hailey & Craig (1995).

#### A.8. RX J0007.0+7302 in CTA 1

An x-ray point source within a pulsar wind nebula in a composite SNR. No pulsations are detected but the general morphology of the object makes it very similar to Vela, including a very likely association with the EGRET  $\gamma$ -ray source 3EG J0010+7309. The x-ray spectrum of the point source, from either *XMM-Newton* (Slane et al. 2004a) or *Chandra* (Halpern et al. 2004), is fitted by a power law plus a thermal component. The latter could be either originating from a hot polar cap or the cooler entire stellar surface. The upper value for the thermal luminosity we use is from Halpern et al. (2004), because the high angular resolution of *Chandra* allows a better estimate than the *XMM-Newton* data. Distance and kinematic age estimates are taken from Slane et al. (2004a).

#### A.9. PSR 0833-45 (Vela)

Spectral fitting from *Chandra* for both H atmosphere and blackbody surfaces are from Pavlov et al. (2001), and the spindown age is also quoted there. The kinematic age of the SNR is from Aschenbach, Egger & Trümper (1995) and the VLBI interferometric distance measurement of 250 pc is due to Dodson et al. (2003). This is probably the most reliable data point available and the first isolated neutron star whose radius is well determined because of a well known distance (Page, Shibano & Zavlin 1996).

#### A.10. PSR 1706+44

Blackbody spectral fitting for the *Chandra* data is from Gotthelf, Halpern & Dodson (2002), and spindown age is quoted in the same source whereas H atmosphere spectral fitting for the *XMM-Newton* data is from McGowan et al (2004). Estimates of distance are from Taylor & Cordes (1993) and Koribalski et al. (1995).

#### A.11. PSR 0538+2817

We employ the results of spectral fitting from *Chandra* by Marshall & Schulz (2002) for both blackbody and magnetized hydrogen models. We assume a typical error of 0.1 on  $\log_{10} T$  and of 0.5 on  $\log_{10} L$ , since these authors do not report any uncertainty estimates.

#### A.12. PSR J0154+61

We use the results of an *XMM-Newton* observation by Gonzalez et al. (2004) for  $L_\infty$ . The distance and  $t_{sd}$  values are taken from the same paper.

#### A.13. PSR 0656+14

We employ the results of spectral fitting from *Chandra* (Marshall & Schulz 2002), which result in a lower temperature than the ROSAT value  $\log_{10} T_\infty = 5.96^{+0.02}_{-0.03}$  quoted by Possenti, Mereghetti & Colpi (1996). Marshall & Schulz (2002) also suggest there is a hard component with a temperature of  $2 \times 10^6$  K. The spindown age is from Taylor, Manchester & Lyne (1993). As with other objects in this study, we employ the softer component's temperature as being more characteristic of the underlying surface temperature. The distance to this object is constrained by the VLBA parallax measurement of Briskin et al. (2003).

#### A.14. PSR 0633+1748 (Geminga)

Blackbody spectral fitting with ROSAT data is from Halpern & Wang (1997); later analyses have not changed these results significantly. The distance is the result of parallax measurements by Caraveo et al. (1996); however, Pavlov (2002) suggests these measurements may not be reliable.

#### A.15. PSR 1055-52

Pavlov (2002) quotes results from *Chandra* observations of two thermal components: a soft component with temperature  $8.9 \pm 0.01 \times 10^5$  K and emitting radius  $13d_{1000}$  km and a hard component with temperature

$1.9 \pm 0.1 \times 10^6$  K and emitting radius of  $0.5 \pm 0.1 d_{1000}$  km. These temperatures are consistent with ASCA results quoted in Greiveldinger et al. (1996) and ROSAT results in Ögelman (1995). We employ the soft component temperature as being characteristic of the average surface temperature.

#### A.16. RX J1856-3754

Absence of spectral lines in the high resolution *Chandra* LETGS data rules out non-magnetic, non-rotating heavy element atmosphere models (Burwitz et al. 2001). Blackbodies provide the best fits to the x-ray data but the optical data require the presence of a colder blackbody component (Pons et al. 2002). We take the blackbody spectral fitting from Drake et al. (2002) and Burwitz et al. (2003) for the warm component and fits for the colder component from Pons et al. (2002). The range of  $T_\infty$  listed in Table 2 correspond to these two, cold and warm, components. The cold blackbody component gives the lower bound on the radius but it makes a very small contribution ( $\sim 5\%$ ) to the luminosity.

#### A.17. RX J0720.4-3125

As for RX J1856-3754, fit of both the x-ray and optical data requires a two blackbody model. We take both warm and cold blackbody fits from Kaplan et al. (2003) which gives us the range of  $T_\infty$  we report in Table 2. The luminosity has a significant contribution from the cold component. The distance is unknown and the values we report are a guess based on the observed low absorption of the x-ray spectrum. This distance results in a large uncertainty in  $L_\infty$ . Notice also that the spectrum is known to vary on long time scales (de Vries et al. 2004) and contains a phase-dependent absorption line (Haberl et al. 2004). Both  $P$  and  $\dot{P}$  are from Cropper et al. (2004).

### B. The Equations of Structure and Evolution

We employ the standard structure equations derived from spherically symmetric, general relativistic, considerations. It should be mentioned that the stellar surface in our computation is fixed by

$$R = R_{\text{star}} = r(\rho = \rho_b), \quad (\text{B1})$$

where  $\rho_b = 10^{10} \text{ g cm}^{-3}$ . This guarantees that the EOS is temperature independent. The layers at densities below  $\rho_b$ , called the *envelope*, are treated separately (see § 4).

At the temperatures of interest here, neutrinos have a mean free path much larger than the radius of the star (Shapiro & Teukolsky (1983)) and thus leave the star once they are produced. Energy balance arguments (see for instance Thorne (1966)) then imply

$$\frac{d(l e^{2\Phi})}{dr} = - \frac{4\pi r^2 e^\Phi}{\sqrt{1 - 2Gm/c^2 r}} \left( \frac{d\epsilon}{dt} + e^\Phi (q_\nu - q_h) \right), \quad (\text{B2})$$

where  $\Phi$  is the gravitational potential,  $l$  is the internal luminosity,  $\epsilon$  is the internal energy per unit volume,  $q_\nu$  and  $q_h$  are respectively the neutrino emissivity and heating rate, both per unit volume. The corresponding inner boundary condition for  $l$  is

$$l(r = 0) = 0 \quad (\text{B3})$$

The time derivative of  $\epsilon$  can be written in the form

$$\frac{d\epsilon}{dt} = \frac{d\epsilon}{dT} \cdot \frac{dT}{dt} = c_v \cdot \frac{dT}{dt}, \quad (\text{B4})$$

where  $T$  is the local temperature and  $c_v$  is the specific heat per unit volume at constant volume, which for degenerate matter is the same as the specific heat at constant pressure  $c_P$ .

The energy transport equation is

$$\frac{d(Te^\Phi)}{dr} = -\frac{1}{\lambda} \frac{le^\Phi}{4\pi r^2 \sqrt{1 - 2Gm/c^2 r}}, \quad (\text{B5})$$

where  $\lambda$  is the thermal conductivity. (Notice that within the relativistic framework, an ‘isothermal’ configuration is defined by  $e^\Phi \cdot T = \text{constant}$ , instead of  $T = \text{constant}$ .) The associated boundary condition is

$$T_b = T_b(l_b), \quad (\text{B6})$$

which relates the temperature  $T_b$  at the outer boundary (defined more precisely further below) to the luminosity  $l_b$  in this layer. The location of this outer boundary layer is chosen such that  $l_b$  is equal to the total photon luminosity of the star,  $l_b = l(r = R) \equiv L$ .  $L$  is commonly expressed through the “effective” temperature  $T_e$ , which is *defined* by

$$L \equiv 4\pi R^2 \cdot \sigma_{SB} T_e^4 \quad (\text{B7})$$

where  $\sigma_{SB}$  is the Stefan-Boltzmann constant. We emphasize that  $L$  and  $T_e$  are, modulo  $R$ , essentially equivalent quantities. We can thus write equation (B6) as  $T_b = T_b(T_e)$ ; this ‘ $T_e - T_b$  relationship’ is discussed further in § 4.

We will present our results of thermal evolution by using the “effective temperature at infinity”

$$T_e^\infty \equiv T_e \cdot e^{\Phi(R)} \quad (\text{B8})$$

related to the “luminosity at infinity”  $L^\infty$  through the “radiation radius”  $R_\infty \equiv R \cdot e^{-\Phi(R)}$  by

$$L^\infty \equiv e^{2\Phi(R)} L(R) = 4\pi R_\infty^2 \cdot \sigma_{SB} T_e^{\infty 4}. \quad (\text{B9})$$

The three quantities  $T_e^\infty$ ,  $L^\infty$  and  $R_\infty$ , are, in principle, measurable. In particular,  $R_\infty$  would be the areal radius of the star that an observer ‘at infinity’ would measure with an extremely high angular resolution instrument (Page 1995).

## REFERENCES

- Ainsworth, T. L., Wambach, J., & Pines, D. 1989, *Phys. Lett.*, B222, 173
- Ainsworth, T. L., Wambach, J., & Pines, D. 1991, in *Neutron Stars: Theory and Observation*, ed. J. Ventura, & D. Pines (Dordrecht: Kluwer) 37
- Akmal, A., & Pandharipande, V. R. 1997, *Phys. Rev.*, C56, 2261
- Akmal, A. and Pandharipande, V. R., & Ravenhall, D. G. 1998, *Phys. Rev.*, C58, 1804,
- Amundsen, L., & Østgaard, E. 1985a, *Nucl. Phys.*, A437, 487
- Amundsen, L., & Østgaard, E. 1985b, *Nucl. Phys.*, A442, 163
- Aschenbach, B., Egger, R., & Trümper, J. 1995, *Nature*, 373, 587
- Babu, S., & Brown, G. E. 1973, *Ann. Phys.*, 78, 1
- Baldo, M., Cugnon, J., Lejeune, A., & Lombardo, U. 1992, *Nucl. Phys.*, A536, 349
- Baldo, M., Elgarøy, Ø., Engvik, L., Hjorth-Jensen, M., & Schulze, H.-J. 1998, *Phys. Rev.*, C58, 1921
- Bardeen, J., Cooper, L. N., & Schrieffer, J. R. 1957, *Phys. Rev.*, 108, 1175
- Barranco, F., Broglia, R. A., Esbensen, H., & Vigezzi, E. 1997, *Phys. Lett.*, B390, 13
- Baym, G., & Pethick, C. 1975, *Ann. Rev. Nucl. Sci.*, 25, 27
- Bezchastnov, V. G., Haensel, P., Kaminker, A. D., & Yakovlev, D. G. 1997, *A&A*, 328, 409
- Bowyer, S., Byran, E. T., Churb, T. A., & Friedman, H. 1964, *Nature*, 201, 1307
- Briskin, W. F., Thorsett, S. E., Golden, A., & Goss, W. M. 2003, *ApJ*, 593, L89
- Burrows, A., & Lattimer, J. M. 1986, *ApJ*, 307, 178
- Burwitz, V., Zavlin, V. E., Neuhauser, R., Predehl, P., Trümper, J., & Brinkman, A. C. 2001, *A&A*, 379, L35
- Burwitz, V., Haberl, F., Neuhauser, R., Predehl, P., Trümper, J., & Zavlin, V. E. 2003, *A&A*, 399, 1109
- Camilo, F., Manchester, R. N., Baensler, B. M., Lorimer, D. R., & Sarkissian, J. 2002, *ApJ*, 567, L71
- Caraveo, P. A., Bignami, G. F., Mignani, R., & Taff, L. G. 1996, *ApJ*, 461, L91
- Chao, N.-C., Clark, J. W., & Yang, C.-H. 1972, *Nucl. Phys.*, A179, 320
- Chabrier, G., Potekhin, A. Y., & Yakovlev, D. G. 1997, *ApJ*, 477, L99
- Chang, P., & Bildsten, L. 2003a, *ApJ*, 585, 464
- Chang, P., & Bildsten, L. 2003b, *astro-ph/0312589*
- Chen, J. M. C., Clark, J. W., Davé, R. D., & Khodel, V. V. 1993, *Nucl. Phys.*, A555, 59
- Clark, J. W., Källman, C.-G., Yang, C.-H., & Chakkalakal, D. A. 1976, *Phys. Lett.*, 61B, 331
- Cooper, L. N. 1956, *Phys. Rev.*, 104, 1189
- Cropper, M., Haberl, F., Zane, S., & Zavlin, V. E. 2004, *MNRAS*, 351, 1099
- de Vries, C. P., vink, J., Méndez, M., & Verbunt, F. 2004, *A&A* 415, L34
- Dodson, R., Legge, D., Reynolds, J. E., & McCulloch, P. M. 2003, *ApJ*, 596, 1137
- Drake, J. J., Marshall, H. L., Dreizler, S., Freeman, P. E., Fruscione, A., Juda, M., Kashyap, V., Nicastro, F., Pease, D., Wargelin, B. J., & Werner, K. 2002, *ApJ*, 572, 996
- Elgarøy, Ø., Engvik, L., Hjorth-Jensen, M., & Osnes, E. 1996, *Nucl. Phys.*, A604, 466
- Elgarøy, Ø., Engvik, L., Hjorth-Jensen, M., & Osnes, E. 1996, *Nucl. Phys.*, A607, 425
- Engvik, L., Hjorth-Jensen, M., Osnes, E., Bao, G., & Østgaard, E. 1994, *Phys. Rev. Lett.*, 73, 2650
- Flowers, E., Ruderman, M., & Sutherland, P. 1976, *ApJ*, 205, 541

- Friman, B. L., & Maxwell, O. V. 1979, *ApJ*, 232, 541
- Green, D. A., & Gull, S. F. 1982, *Nature*, 299, 606
- Geppert, U., Kuecker, M., & Page, D. 2004, submitted to *A&A* [astro-ph/0403441]
- Giacani, E. B., Dubner, G. M., Green, A. J., Goss, W. M., & Gaensler, B. M. 2000, *AJ*, 119, 281
- Gonzalez, M. E., Kaspi, V. M., Lyne, A. G., & Pivovarov, M. J. 2004, *ApJ*, 610, LXXX (in press)
- Gotthelf, E. V., Halpern, J. P., & Dodson, R. 2002, *ApJ*, 567, L125
- Greiveldinger, C., Camerini, U., Fry, W., Markwardt, C. B., Ögelman, H., Safi-Harb, S., Finley, J. P., Tsuruta, S., Shibata, S., Sugawara, T., Sano, S., & Tukahara, M. 1996, *ApJ*, 465, L35
- Greenstein, G., & Hartke, G. J. 1983, *ApJ*, 271, 283
- Gudmundsson, E. H., Pethick, C. J., & Epstein, R. I. 1982, *ApJ*, 259, L19
- Gudmundsson, E. H., Pethick, C. J., & Epstein, R. I. 1983, *ApJ*, 272, 286
- Gusakov, M. E., Kaminker, A. D., Yakovlev, D. G., & Gnedin, O. Y. 2004, Submitted to *A&A* [astro-ph/0404002]
- Haberl, F., Motch, C., Buckley, D. A. H., Zickgraf, F. J., & Pietsch, W. 1997, *A&A*, 326, 662
- Haberl, F., Zavlin, V. E., Trümper, J., & Burwitz, V. 2004, *A&A*, 419, 1077
- Haensel, P., Zdunik, J. L., & Dobaczewski, J. 1989, *A&A*, 222, 353
- Haft, M., Raffelt, G., & Weiss, A. 1994 *ApJ*, 425, 222
- Hailey, C. J., & Craig, W. W. 1995, *ApJ*, 455, L151
- Halpern, J. P., Gotthelf, E. V., Camilo, F., & Helfand, D. F. 2004, submitted to *ApJ*, astro-ph/0404312
- Halpern, J. P., & Wang, F. Y.-H. 1997, *ApJ*, 477, 905
- Hambaryan, V., Hasinger, G., Schwope, A. D., & Schulz, N. S. 2002, *A&A*, 381, 98
- Hanhart, C., Phillips, D. R., & Reddy, S. 2001, *Phys. Lett.*, B499, 9
- Hernquist, L., & Applegate, J. H., 1984, *ApJ*, 287, 244
- Hoffberg, M., Glassgold, A. E., Richardson, R. W., & Ruderman, M. 1970, *Phys. Rev. Lett.*, 24, 775
- Horowitz, C. J., & Piekarewicz, J. 2001, *Phys. Rev. Lett.*, 86, 5647
- Hughes, J. P., Slane, P. O., Park, S., Roming, P. W. A., & Burrows, D. N. 2003, *ApJ*, 591, L139
- Itoh, N., Hayashi, H., Nishikawa, A., & Kohyama, Y. 1996, *ApJS*, 102, 411
- Jackson, A. D., Krotscheck, E., Meltzer, D. E., & Smith, R. A. 1982, *Nucl. Phys.*, A386, 125
- Kaminker, A. D., Haensel, P., & Yakovlev, D. G. 2001, *A&A*, 373, L17
- Kaminker, A. D., Pethick, C. J., Potekhin, A. Y., Thorsson, V., & Yakovlev, D. G. 1999, *A&A*, 343, 1009
- Kaminker, A. D., Yakovlev, D. G., & Gnedin, O. Y. 2002, *A&A*, 383, 1076
- Kaplan, D. L., Kulkarni, S. R., van Kerkwijk, M. H., & Marshall, H. 2002, *ApJ*, 570, 79
- Kaplan, D. L., van Kerkwijk, M. H., Marshall, H. L., Jacobi, B. A., Kulkarni, S. R., & Frail, D. A. 2003, *ApJ*, 590, 1008
- Kaplan, D. L., Frail, D. A., Gaensler, B. M., Gotthelf, E. V., Kulkarni, S. R., Slane, P. O., & Nechita, A. 2004, *ApJS*, 153, 269
- Kippenhahn, R., & Weigert, A., *Stellar Structure and Evolution*, (A&A Library, Springer Verlag: Berlin) 1990
- Koribalski, B., Johnston, S., Weisberg, J. M., & Wilson, W. 1995, *ApJ*, 441, 756
- Lattimer, J. M., Pethick, C. J., Prakash, M., & Haensel, P. 1991, *Phys. Rev. Lett.*, 66, 2701

- Lattimer, J. M., & Prakash, M., 2001 ApJ, 550, 426
- Levenfish, K. P., & Yakovlev, D. G. 1994a, Astron. Rep., 38, 247
- Levenfish, K. P., Shibano, Y. A., & Yakovlev, D. G. 1999, Astron. Lett., 25, 417
- Marshall, H. L., & Schulz, N. S. 2002, ApJ, 574, 377
- McAdam, W. B., Osborne, J. I., & Parkinson, M. L. 1993, Nature, 361, 516
- McGowan, K. E., et al. 2004, ApJ, 600, 343
- Mereghetti, S., Bignami, G. F. & Caraveo, P. A. 1996, ApJ, 464, 842
- Mereghetti, S., De Luca, A., Caraveo, P. A., Becker, W., Mignami, R., & Bignami, G. F. 2002, ApJ, 581, 1280
- Mereghetti, S., Tiengo, A., & Israel, G. L. 2002 ApJ, 569, 275
- Misner, C., Thorne, K., & Wheeler, J. A., Gravitation, (San Francisco: Freeman) 1973
- Morton, D. D. 1964, Nature, 201, 1308
- Motch, C., Zavlin, V. E., & Haberl, F. 2003, A&A, 408, 323
- Murray, S. S., et al. 2002, ApJ, 568, 226
- Müther, H., Prakash, M., & Ainsworth, T. L. 1987, Phys. Lett., B199, 469
- Muzikar, P., Sauls, J. A., & Serene, J. W. 1980, Phys. Rev., D21, 1494
- Müller, H., & Serot, B. D. 1996, Nucl. Phys., A606, 508
- Negele, J. W., & Vautherin, D. 1973, Nucl. Phys., A207, 298
- Niskanen, J. A., & Sauls, J. A. 1981, preprint
- Nomoto, K., & Tsuruta, S. 1987, ApJ, 312, 711
- Ögelman, H. 1995, in Proc. NATO ASI on the Lives of Neutron Stars, ed. A. Alpar, Ü. Kiziloğlu & J. van Paradijs (Dordrecht: Kluwer), 101
- Page, D. 1989, Ph.D. dissertation, SUNY at Stony Brook
- Page, D. 1995, ApJ, 442, 273
- Page, D. 1998, in Proc. NATO ASI on The Many Faces of Neutron Stars, ed. R. Bucheri, J. van Paradijs, and M. A. Alpar (Dordrecht: Kluwer), 539
- Page, D., & Sarmiento, A. 1996 ApJ, 473, 1067
- Page, D., Shibano, Y. A., & Zavlin, V. E. 1996, in Roentgenstrahlung from the Universe, ed. H. U. Zimmermann, J. E. Trümper, & H. Yorke (MPE Rep. 263; Munich: MPE), 173 [astro-ph/9601187]
- Pavlov, G. G. 2000, talk at the Santa Barbara KITP program on “Spin and Magnetism in Young Neutron Stars”
- Pavlov, G. G. 2002, astro-ph/0305454
- Pavlov, G. G., & Zavlin, V. E. 2002, in Proc. XXI Texas Symp. on Rel. Astrophys. [astro-ph/0305454]
- Pavlov, G. G., Zavlin, V. E., Aschenbach, B., Trümper, J., & Sanwal, D. 2000, ApJ, 531, L53
- Pavlov, G. G., Zavlin, V. E., & Sanwal, D. 2002, in Neutron stars, Pulsars and Supernova Remnants, ed. W. Becker, H. Lesch, & J. Trümper (MPE Rep. 278; Munich: MPE), 283 [astro-ph/0206024]
- Pavlov, G. G., Zavlin, V. E., Sanwal, D., Burwitz, V., & Garmire, G. P. 2001 APJ, 552, L129
- Pavlov, G. G., Zavlin, V. E., Sanwal, D., & Trümper, J. 2002, ApJ, 569, L95
- Pethick, C. J. 1992, Rev. Mod. Phys., 64, 1133
- Pines, D. 1971, in Proc. XII Int. Conf. on low temperature physics, ed. E. Kandu (Tokyo: Kligatu)
- Pons, J. A., Walter, F. M., Lattimer, J. M., Prakash, M., Neuhäuser, R., & An, P. 2002, ApJ, 564, 981
- Possenti, A., Mereghetti, S., & Colpi, M. 1996, A&A, 313, 565

- Potekhin, A. Y., Chabrier, G., & Yakovlev, D. G. 1997, *A&A*, 323, 415
- Potekhin, A. Y., & Yakovlev, D. G. 2001, *A&A*, 374, 213
- Potekhin, A. Y., Yakovlev, D. G., Chabrier, G., & Gnedin, O. Y. 2003, *ApJ*, 594, 404
- Prakash, M., Prakash, Manju., Lattimer, J. M., & Pethick, C. J. 1992, *ApJ*, 390, L77
- Prakash, M. 1998, in *Nuclear and Particle Astrophysics*, ed. J. G. Hirsch, & D. Page (Cambridge: Cambridge University Press), 153
- Prakash, M., Bombaci, I., Prakash, Manju., Lattimer, J. M., Ellis, P.J., & Knorren, R. 1997, *Phys. Rep.*, 280, 1
- Roberts, D. A., Goss, W. M., Kalberla, P. M. W., Herbstmeier, U., & Schwarz, U. J. 1993, *A&A*, 274, 427
- Roger, R. S., Milne, D. K., Kesteven, M. J., Wellington, K. J., & Haynes, R. F. 1988, *ApJ*, 332, 940
- Romani, R. W. 1987, *ApJ*, 313, 718
- Sanwal, D., Pavlov, G. G., Zavlin, V. E., & Teter, M. A. 2002, *ApJ*, 574, L61
- Schaab, C., Sedrakian, A., Weber, F., & Weigel, M. K. 1999, *A&A*, 346, 465
- Schaab, C., Weber, F., Weigel, M. K., & Glendenning N. K. 1996, *Nucl. Phys.*, A605, 531
- Schaab, C., Voskresensky, D., Sedrakian, A. D., Weber, F., & Weigel, M. K. 1997, *A&A*, 321, 591
- Schulze, H.-J., Cugnon, J., Lejeune, A., Baldo, M., & Lombardo, U. 1996, *Phys. Lett.*, B375, 1
- Schwenk, A., Friman, B., & Brown, G. E. 2003, *Nucl. Phys.*, A713, 191
- Schwenk, A., & Friman, B. 2004, *Phys. Rev. Lett.*, 92, 082501
- Schwenk, A., Jaikumar, P., & Gale, C. 2004 *astro-ph/0309072*
- Shapiro, S. L., & Teukolsky, S. A. *Black Holes, White Dwarfs, and Neutron Stars* (New York: John Wiley & Sons) 1983
- Slane, P. O., Helfand, D. J., & Murray, S. S. 2002, *ApJ*, 571, L45
- Slane, P., Zimmerman, E. R., Hughes, J. P., Seward, F. D., Gaensler, B. M., & Clarke, M. J. 2004 *ApJ*, 601, 1045
- Slane, P., Helfand, D. J., van der Swaluw, E., & Murray, S. S. 2004, submitted to *ApJ* [*astro-ph/0405380*]
- Steiner, A. W., Prakash, M., Lattimer, J. M., & Ellis, P. J. To be published (2004)
- Takatsuka, T. 1972a, *Prog. Theor. Phys.*, 47, 1062
- Takatsuka, T. 1972b, *Prog. Theor. Phys.*, 48, 1517
- Takatsuka, T. 1973, *Prog. Theor. Phys.*, 50, 1754
- Tamagaki, R. 1970, *Prog. Theor. Phys.*, 44, 905
- Taylor, J. H., & Cordes, J. M. 1993, *ApJ*, 411, 674
- Taylor, J. H., Manchester, R. N., & Lyne, A. G. 1993, *ApJS*, 88, 529
- Thorne K. *High Energy Astrophysics* (New York: Gordon Breach) 1966
- Tsuruta, S., Teter, M. A., Takatsuka, T., Tatsumi, T., & Tamagaki, R. 2002, *ApJ*, 571, L143
- Umeda, H., Shibazaki, N., Nomoto, K., & Tsuruta, S. 1993, *ApJ*, 408, 186
- Urpin, V. 2004, *A&A*, 421, L5
- Van Dalen, E. N. E., Dieperink, A. E. L., & Tjon, J. A. 2003, *Phys. Rev.*, C68, 064307
- van Riper, K. A. 1988, *ApJ*, 329, 339
- Voskresensky, D. N., & Senatorov, A. V. 1986, *Sov. Phys. JETP*, 63, 885
- Voskresensky, D. N., & Senatorov, A. V. 1987, *Sov. J. Nucl. Phys.*, 45, 411
- Wald, R. M., *General Relativity*, (Chicago: Chicago University Press) 1984
- Walter, F. M., & Lattimer, J. M. 2002, *ApJ*, 576, L145



- Wambach, J., Ainsworth, T. L., & Pines, D. 1993, Nucl. Phys., A555, 128
- Wiringa, R. B. 1988, Phys. Rev., C38, 2967
- Wiringa, R. B., Fiks, V., & Fabrocini, A. 1988, Phys. Rev., C38, 1010
- Yakovlev, D. G., Kaminker, A. D., & Gnedin, O. Y. 2001, A&A, 379, L5
- Yakovlev, D. G., & Haensel, P. 2003, A&A, 407, 259
- Yakovlev, D. G., & Levenfish, K. P. 1995, A&A, 297, 717
- Yakovlev, D. G., & Pethick, C. J. 2004, ARA&A, to be published.
- Yakovlev, D. G., Kaminker, A. D., Haensel, P., & Gnedin, O. Y. 2002, A&A, 389, L24
- Zavlin, V. E., & Pavlov, G. G.
- Zavlin, V. E., Pavlov, G. G., & Sanwal, D. 2004, ApJ, 604, 444
- Zavlin, V. E., Pavlov, G. G., Sanwal, D., & Trümper, J. 2000, ApJ, 540, L25
- Zavlin, V. E., Pavlov, G. G., & Trümper 1998, A&A, 331, 821
- Zavlin, V. E., Trümper, J., & Pavlov, G. G. 1999, ApJ, 525, 959
- Zverev, M. V., Clark, J. W., & Khodel, V. A. 2003, Nucl. Phys., A720, 20